MOLECULAR MECHANISMS OF THE COUPLING OF GATING TO VOLTAGE SENSING IN TRANSMEMBRANE PROTEINS

Inauguraldissertation

zur

Erlangung der Würde eines Doktors der Philosophie

vorgelegt der

Philosophisch-Naturwissenschaftlichen Fakultät

der Universität Basel von

Gregory Weber Starek

aus den Vereinigte Staaten von Amerika

Basel, 2016

Genehmigt von der Philosophisch-Naturwissenshaftlichen Fakultät

auf Antrag von

(Prof. Dr. Simon Bernèche) Principal Adviser

Genehmigt von der Philosophisch-Naturwissenshaftlichen Fakultät

auf Antrag von

(Prof. Dr. Roderick Lim)

Genehmigt von der Philosophisch-Naturwissenshaftlichen Fakultät

auf Antrag von

(Prof. Dr. Jörg Schibler)

Basel, 25 March, 2014

For my family.

Acknowledgments

First and foremost, I must thank my advisor, Simon Bernèche. From our earliest email exchanges nearly six years ago, Simon's passion for science, dedication to his lab, and overwhelmingly friendly disposition made it clear that he would make an ideal advisor. His remarkable curiosity, attention to detail, and relentless persistence have been both a giant pain and, more importantly, a tremendous and immeasurable asset in my development as a scientist. I cannot thank him enough for giving me the opportunity to learn from him, and also for all of his immeasurable patience (something he probably learned from being a Canadiens fan). I'm a better scientist and a better man for having worked with him.

Somehow I was lucky enough to find myself with a second advisor, Doug Tobias. I am eternally grateful to Doug for opening his lab to me. His enthusiasm for science, mastery of incredibly diverse subject matter, and effortless ability to communicate and articulate even the most intricate and complex scientific problems are traits that I will spend my entire career trying to match. I cannot thank him enough for never getting too mad when I

used up all of the computer time, the perfectly-timed kick in the butt, and, above all else, for bringing me home.

The second half of my PhD work would not have been possible without the help of Alfredo Freites, whose experience and expertise is absolutely second to none. Somehow–and I never knew that this was possible–Alfredo has made my work easier, my results cleaner and more reliable, and also made the lab a better place to be. I am both a much better coder and a much better scientist than I was upon my arrival to UC Irvine, and so much of this is the direct result of having worked with Alfredo.

A great deal of my work has been inspired by incredibly talented scientists. I cannot thank my PhD committee members, Markus Meuwly and Roderick Lim, enough for their thoughtful criticisms and contributions to my PhD work, as well as for making graduate lectures an enjoyable and productive experience. My position at UC Irvine has allowed me the unique and enviable opportunity to participate in the TEMPO group with Steve White, Jim Hall, Francesco Tombola, Melanie Cocco, Kent Blasie, and Alexey Ladokhin, among so many others. It has been an honor to sit in on meetings with scientists whose names and reputations I knew long before my arrival in Irvine. Much of the work presented here has benefitted from fruitful collaborations with talented experimentalists. Chapter 3 would not be possible without the incredibly thorough work of Elise Faure, Hugo McGuire, and

Rikard Blunck. Chapter 5 was made possible by the tireless (and endless) work of Mihaela Mihailescu, Dmitry Krepkiy, Mirela Milescu, Klaus Gawrisch, Kenton Swartz, and Steve White. I am also extremely grateful for the contributions from past and present group members in Irvine and Basel, including Matthias Heyden, Abe Stern, Olivier Bignucolo, Florian Heer, and Yanyan Xu.

My biggest fear upon entering grad school was being forced to share an office with someone for four and a half years. To my surprise, and to my incredible, incredible luck, I somehow found myself sharing space with some of the best and brightest people I have ever known. In Irvine, I will forever be thankful to Mona Wood for sharing everything from her project to her textbooks with me, for tolerating two years of dim (i.e. better) lighting, and for always being willing to help whenever I needed it. In Basel, I am eternally grateful for my officemates Céline Boiteux, Sefer Baday, and Wojciech Wojtas-Niziurski. Not only did these three improve the quality of my research, but also the quality of each and every day I spent in Basel. For all of the rollercoaster rides, concerts, YouTube distractions, movie nights, drinks after work, long lunches at the Rhein, IKEA furniture assembly, and the absolutely absurd amount of Thai food we ate together, thank you. I am unbelievably fortunate to have been able to count them among my colleagues during my PhD studies, and I am even luckier to be able to count them among my lifelong friends. I am also especially thankful for Yvonne Steger and Rita Manohar, who not only made two transatlantic moves possible, but also (and more importantly) helped make Switzerland a new home for me.

Simply put, there are no greater ambassadors for the Biozentrum, the city of Basel, and the country of Switzerland than Yvonne and Rita.

This dissertation, like biology, did not occur in a vacuum. I most certainly would not be here had it not been for John Mottes, my high school biology teacher, whose class introduced me to the molecular world, which began as a curiosity and has now brought me from harmonic oscillations of carbon atoms to a new home in Southern California, a year in Sweden, higher education in Switzerland, conferences on multiple continents, and, I hope, much more in the future. I am also forever indebted to Christy Moroye, who, for the past fifteen years, has known me better than I know myself. Her encouragement and support during my most impressionable years has helped shape me into the man that I am proud to be today. I am also eternally grateful for the Harmacek family for always looking out for me, and for always welcoming me into their home. Of course, I must also thank Chipotle and KCRW for fueling me throughout my graduate studies.

Perhaps the greatest surprise of my PhD studies was the opportunity to spend two years in Newport Beach, and I must thank Joe Ament, Pete Johns, Nick Paloukos, and Casey Skinner for sharing the experience and their home with me. Having to live with roommates can be torture, but these three have made the past two years more fun than I could have ever imagined. Always up for a bike ride, a beach afternoon, a Sunday brunch, or a game

of basketball, I have never felt more at home in California than I have on 40th Street. Gentlemen, I thank you.

I am extremely fortunate to be surrounded by amazing people outside of work, too numerous to mention here. Over the past ten years, I've watched my friends transform into doctors, lawyers, teachers, academians, writers, police officers, and so much more. It is an honor to count you among my friends, and I cannot wait to see what you continue to accomplish in the future. To everyone over the past five years who has provided support, lent me their couch for a night, sweat and bled for a Swiss football championship, offered advice, or just shared a beer with me, thank you. It has meant the world to me.

And finally, to my family: thank you. Thank you, thank you, thank you. For twenty nine years of unrelenting love, support, encouragement, motivation, and inspiration, thank you. This accomplishment is as much yours as it is mine.

Convention dictates that this chapter be titled "Acknowledgments," and, for fear of running afoul of university regulations (because—let's be honest—the official regulations far exceed my German translation skills), I have elected to uphold this tradition. For this, I am truly sorry. You deserve so much more. An acknowledgment is a platitude—a mere admission of familiarity. For this work, a more apt chapter title would be "From the Absolute Bottom of the Very Deepest Part of My Heart, Down to the Very Last Atom, Thank You."

Contents

List of Tables

List of Figures

Chapter 1

Introduction

Voltage gated potassium ion (Kv) channels regulate action potentials of the nervous system by responding to changes in transmembrane voltage, enabling K^+ transport across the membrane to restore cells to their resting potential (Hodgkin and Huxley, 1952; Long et al., 2007). Comprised of four identical subunits, Kv channels contain four voltage sensing domains arranged on the periphery of a central pore domain. Each voltage sensor is comprised of four transmembrane helices, numbered S1 through S4. The S4 helix, containing four to six highly-conserved, positively-charged arginine or lysine residues, is responsible for voltage sensitivity in Kv channels (Papazian et al., 1991; Sigworth, 1994; Bezanilla, 2000). The pore domain consists of two transmembrane helices, S5 and S6. The S5 helix constitutes the periphery of the pore domain and is believed to be relatively immobile. The

S6 helices, lining the interior of the channel, gate the protein and regulate K^+ permeation (Jiang et al., 2003; Long et al., 2005b, 2007). Because each subunit of Kv channels contains six transmembrane helices, they are often referred to as 6TM Kv channels.

The depolarization of an action potential is initiated as sodium ions enter the cell (Hodgkin and Huxley, 1952). At the cellular resting potential of -70 mV, potassium ion channels are closed, and the S4 helix is in its "down" state. As the electrochemical gradient changes, the S4 helices of Kv channels begin to reorient within the membrane. At the peak of the action potential (roughly +20 mV), the S4 helices exist in their "up" state (Jiang et al., 2003). This conformational transition of the S4 helix is coupled to the pore domain via the S4-S5 linker, a short, amphipathic helix along the intracellular membrane-water interface. By bridging the C-terminus of the voltage sensor to the N-terminus of the pore domain, the S4-S5 linker couples the voltage sensitivity of the voltage sensor to K+ conduction in the pore domain (Blunck and Batulan, 2012).

Because they begin opening at voltages less than 0 mV, all crystal structures of Kv channels contain an open pore domain (Jiang et al., 2003; Long et al., 2005b, 2007). With no structure in the closed conformation, the mechanism of gating in Kv channels remains unclear. Nevertheless, significant biophysical studies have revealed insights into both the closed conformation and the gating transition itself (reviewed in Tombola et al., 2006). In

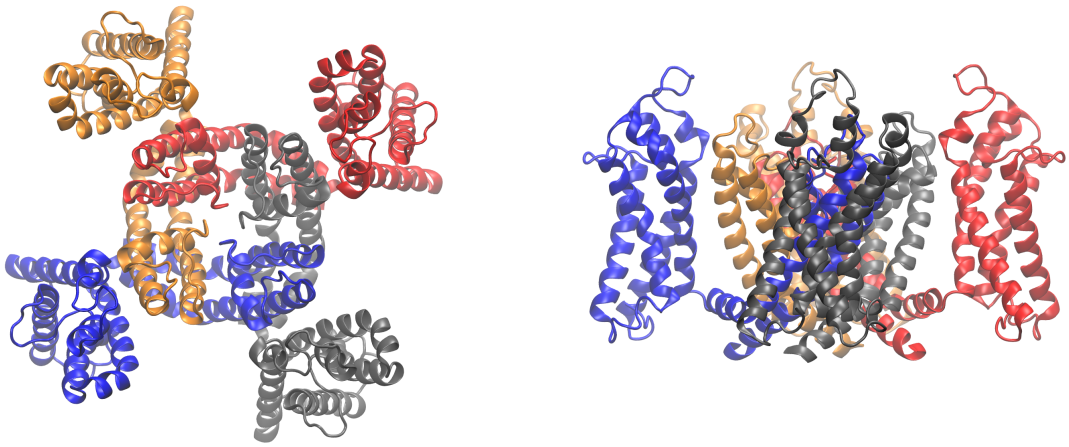

(a) (b)

Figure 1.1: The transmembrane region of the crystal structure of the Kv1.2/2.1 chimera (PDB code 2r9r), viewed extracellularly (a) and from the side (b). The cytoplasmic domain (not shown) is not essential for channel function.

this dissertation, I will explore questions relevant to the gating mechanism in voltage gated potassium ion channels through fully-atomistic molecular dynamics (MD) simulations.

First, in Chapter 2, I will address the potential role of the 3_{10} helical conformation found in the C-terminal end of S4 in the crystal structures of Kv channels. Spanning eight or more residues, these 3_{10} helices are both uncharacteristically long and conserved in K^+ channel crystal structures (Vieira-Pires and Morais-Cabral, 2010). By simulating the Kv1.2/2.1 chimera channel's voltage sensor embedded in a lipid bilayer, I find that an alpha to 3_{10} helical interconversion of the S4 helix reproduces many experimental measurements of the open and closed states of Kv channels.

In Chapter 3, I perform molecular dynamics simulations of the entire Kv1.2/2.1 chimera channel. First, I examine the impact of an alpha to 3_{10} helical interconversion of the S4 helix on the pore domain of the channel. Though the results are consistent with the results in Chapter 2 (and the corresponding experimental measurements), I find that this secondary structural modification is insufficient to influence the pore domain of the channel on the timescale of my simulations. In the second half of Chapter 3, I use molecular dynamics simulations to generate a closed state model of the Kv1.2/2.1 chimera from luminescence resonance energy transfer (LRET) measurements of the closed conformation of KvAP. The resulting structure is indeed closed, and also recapitulates a number of experimentally determined measurements of the closed channel (Faure et al., 2012).

In Chapter 4, I focus on the pore domain. First, using targeted molecular dynamics simulations, I generate a transition between a closed model of the KvAP linker and pore domain to the open conformation. Then, using an umbrella sampling method, I quantify the energetics of the gating transition in KvAP and assess the physiological implications. In agreement with experimental studies of Kv channel energetics, I find that the open pore is roughly 2.7 kcal/mol lower in free energy than the closed conformation. The targeted molecular dynamics and umbrella sampling simulations reveal additional insights into the gating mechanism of KvAP.

Lastly, in Chapter 5, I use MD simulations to gain insights into the binding mechanism of VSTx1, a Kv channel inhibitor. By using the experimentally determined neutron scattering density profile of the VSTx1 toxin bound to a lipid bilayer as a restraint for molecular dynamics simulations, I recreate the experimental scattering density profile, and also offer insight into the binding of VSTx1 to a lipid membrane.

Chapter 2

The 3_{10} Helix in S4 and its Relevance to Gating

2.1 Introduction

The primary actor in the voltage sensitive response of Kv channels is the S4 helix of the voltage sensing domain (Bezanilla, 2000). Sequence alignment of 6TM potassium ion channels reveals four to six highly conserved positively charged arginine and lysine residues at every third residue along S4 (Figure 2.1). Site directed mutagenesis studies

```
AILRVIRLVRVFRIFKLSRHSKGL   Kv1.2
RVVWIFRIMRILRILKLARHSTGL   Kv2.1
GLFRLVRLLRFLRILLIISRGSKF   KvAP
DGSPDWSLYCAVWLLKPLRDSTFF   MlotiK1
```

Figure 2.1: Sequence alignment of the S4 helix in crystal structures of potassium ion channels. Conserved, basic i→i+3 residues are in red.

have shown that these conserved basic residues are responsible for the majority of the voltage sensitivity in Kv channels (Seoh et al., 1996).

X-ray crystal structures of 6TM Kv channels have revealed shared structural motifs beyond mere primary sequences. One such salient similarity is found in the voltage sensor; Kv1.2 and the Kv1.2/2.1 chimera crystal structures, both captured in the open state, contain 3_{10} helices spanning several turns at the C-terminal end of the S4 helix (Long et al., 2005b, 2007). Mlotik1, a 6 TM cyclic nucleotide gated potassium channel, and NavAb, a 6TM voltage gated sodium channel, are both crystalized in the closed state (Clayton et al., 2008; Payandeh et al., 2011), but nevertheless contain 3_{10} helices spanning the entire transmembrane region of S4.

With (ϕ, ψ) dihedral angles of (-49°, -26°), the 3_{10} helix is characterized by hydrogen bonds between the carbonyl of residue i to the amide hydrogen of residue i+3. This unique hydrogen bonding pattern winds the 3_{10} helix more tightly than the i→i+4 hydrogen bonding pattern of the more common alpha helix (Enkhbayar et al., 2006).

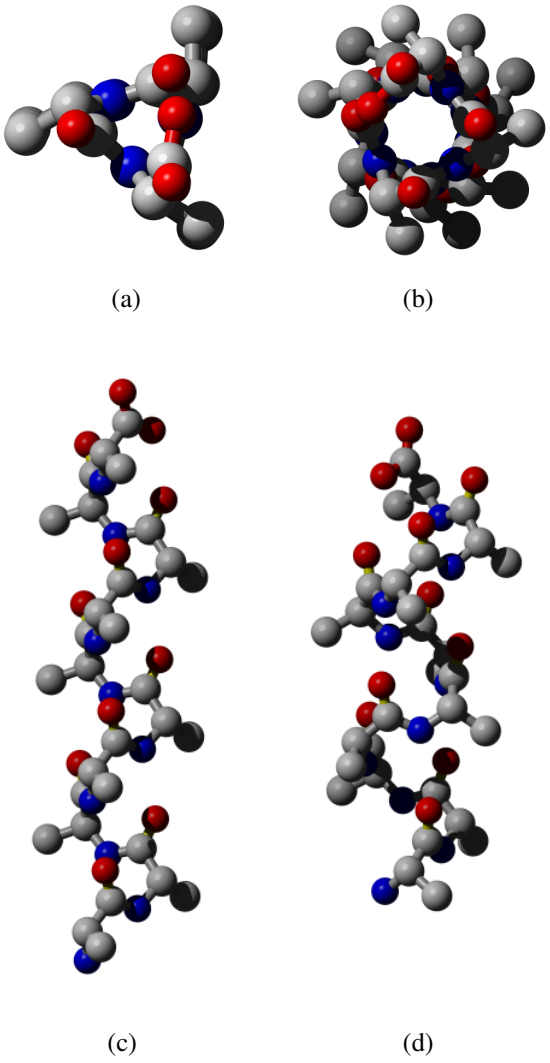

(a) (b)

(c) (d)

Figure 2.2: A decalanine peptide in the 3_{10} (a, c) and alpha (b, d) conformations. Viewed down the helical axis, the 3_{10} conformation (a) is narrower than the alpha helix (b), and inherently stacks the sidechains of the peptide along one of three helical faces. A 90° rotation of the helix reveals that the 3_{10} helix is roughly 30% longer than the alpha conformation.

The structural ramifications of these differing hydrogen bonding patterns are also significant. Canonical 3_{10} helices are approximately 20-30% longer than canonical alpha helices; the length of a 3_{10} helix increases roughly 1.8-2.0 Å per additional residue, while alpha helices increase roughly 1.5 Å per additional residue (Clayton et al., 2008). 3_{10} helices are also narrower than alpha helices; the radius (delimited by the backbone) of a 3_{10} helix is roughly 1.9 Å, while the radius of an alpha helix is roughly 2.3 Å. The i→i+3 bonding pattern of the 3_{10} helix aligns the sidechains of residues i and i+3 along the same helical face, whereas the alpha helix staggers sidechains around the entire face of the helix (Figure 2.2).

The 3_{10} helix is a rare secondary structure element, and 3_{10} helices extending beyond two turns are exceedingly uncommon (Figure 2.3). The paucity of 3_{10} helices has given way to significant discussion about their energetics (Vieira-Pires and Morais-Cabral, 2010). This lack of solid data leads to vast differences in the dihedral energetics of 3_{10} helices in different empirically derived force fields (Patapati and Glykos, 2011). Given the recurrence of the 3_{10} motif in the S4 helix of 6 TM ion channels, their energetic, structural, and functional implications must be considered. The response of S4 to transmembrane voltage has been highly debated, and several models of voltage sensor modification in response to voltage changes have been proposed, consisting of transmembrane translocations, tilts, and twists (reviewed in Tombola et al., 2006). What if the conversion of S4 from an alpha to a 3_{10} conformation were central to the voltage-gating mechanism?

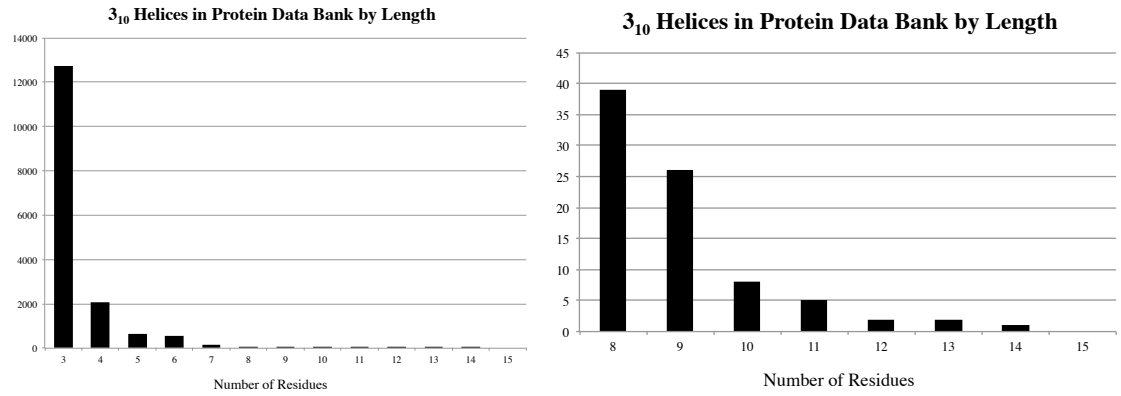

(a) (b)

Figure 2.3: The total number of 3_{10} helices (a) and long (eight or more residues) 3_{10} helices in a selection of 7909 non-redundant protein structures, sorted by length.

To address the possibility of a functional role of the 3_{10} helix in S4 of Kv channels, I have performed fully atomistic MD simulations on the Kv1.2/2.1 chimera voltage sensor with restraints applied to the secondary structure of the S4 helix. The energetic and structural ramifications of an alpha to 3_{10} interconversion are then discussed.

2.2 Methods

Using the CHARMM-GUI web service (Jo et al., 2008), the voltage sensor of the Kv1.2/2.1 chimera (PDB code 2r9r, residues 153 through 315) was embedded in two different bilayers: one composed of DPPC lipids, and a second composed of DLPE lipids (Figure 2.4). These systems were then copied to create three identical systems for each lipid environment with varying S4 structure: 3_{10}, alpha, and wild-type (unrestrained, hereafter abbreviated as

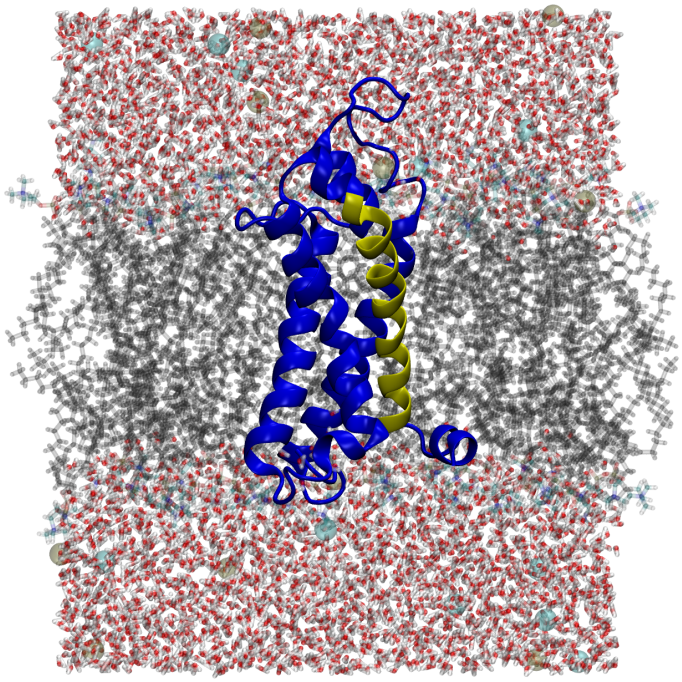

Figure 2.4: The experimental setup for Kv1.2/2.1 chimera simulations in a DPPC membrane. Residues 285 through 305 of the S4 helix, shown above in a 3_{10} helix, are yellow.

WT). To induce helical secondary structure, harmonic distance restraints of 3.0 Å were applied between the carbonyl oxygen atoms of residue i and the amide nitrogen atoms of residue i+3 or i+4 in the 3_{10} and alpha conformations, respectively. The restraints spanned the length of S4 (residues 285 through 305). Additionally, harmonic restraints between the carbonyl oxygens and amide hydrogens of the aforementioned residues were applied at 2.0 Å. The unrestrained system had no restraints applied to control the secondary structure of S4. Though slightly shorter than the canonical hydrogen bond distance, the harmonic potential permits small local conformational flexibility while ensuring the desired secondary structure is maintained throughout the region of interest.

To equilibrate the system, harmonic restraints were applied to the entire protein. These restraints were gradually reduced during 375 ps of equilibration. The S4 secondary structure restraints remained constant.

Molecular dynamics simulations were performed for each of the systems for 100 ns using NAMD 2.8 (Phillips et al., 2005) with the CHARMM27 force field for proteins and phospholipids (MacKerell et al., 1998). Temperature was held constant at 303.15 K with Langevin dynamics, and pressure was held constant at 1 atm with the Langevin Nosé-Hoover method. All simulations were performed with periodic boundary conditions. Water was represented with the TIP3P water molecule, KCl concentration was set to 150 mM, and high frequency hydrogen vibrations were controlled using the SHAKE algorithm. An identical simulation protocol was carried out with the unrestrained voltage sensor using AMBER-99 force field for 20 ns (Wang et al., 2000).

2.3 Results

Distance restraints between atoms within backbone carbonyls and amide groups were sufficient to induce 3_{10} and alpha helix formation, respectively (Fig. 2.5). Because of the more tightly-wound structure of 3_{10} helices, the S4 helix is roughly 4.5 Å longer in the 3_{10} conformation than in the alpha conformation, in line with the canonical definition of a 3_{10}

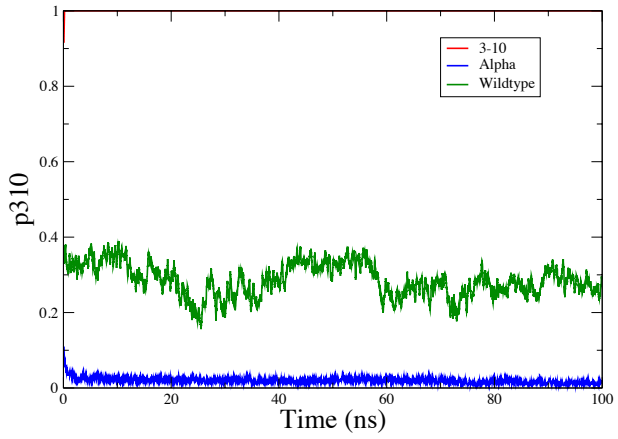

Figure 2.5: The 3_{10} helical propensity of the S4 helix of the 3_{10} , alpha, and wildtype simulations. The i→i+3 distance restraints are sufficient to induce a 3_{10} helical conformation.

helix. The length of the unrestrained S4, which contains a 3_{10} helix at its C-terminal end, is intermediate to the alpha and 3_{10} S4 lengths (Fig. 2.6a), reflecting its intermediate 3_{10} helical content.

Similarly, the tilt angle of the S4 helix with respect to the membrane normal increases as its 3_{10} helical content increases (Fig. 2.6b-c). The S4 helix in the shorter alpha conformation adopts the most vertical orientation within the membrane, while the S4 helix in the 3_{10} conformation tilts farther from the membrane normal. The unrestrained S4 helix is more promiscuous, most frequently visiting orientations similar to the alpha and 3_{10} helices. This bimodal behavior of the unrestrained helix suggests that certain tilt angles within the membrane are more favorable than others, and the secondary structure of the helix can

promote energetically favored orientations within the membrane. The transformation from alpha to 3_{10} helix results in an increase in tilt from the membrane normal of roughly 15°.

This discrepancy in tilt angles between the alpha and 3_{10} conformations of S4 was independent of lipid type. Identical simulations were performed with voltage sensors in both DPPC and DLPE lipids. While the shorter DLPE lipids did increase the tilt of S4 helices by approximately 10°, the lipid length did not affect the disparity between alpha and 3_{10} tilt angles (roughly 15°, Fig. 2.6b-c), Thus, we can conclude that hydrophobic mismatch drives helical tilting to varying degrees depending on the secondary structure of S4.

Salt bridge pairs within the voltage sensor proved to be robust and mostly unaffected by the secondary structure of the S4 helix. Prominent salt bridge pairs found in the Kv1.2/2.1 chimera crystal structure endured in all simulated conformations (Figures 2.7, 2.8, 2.9).

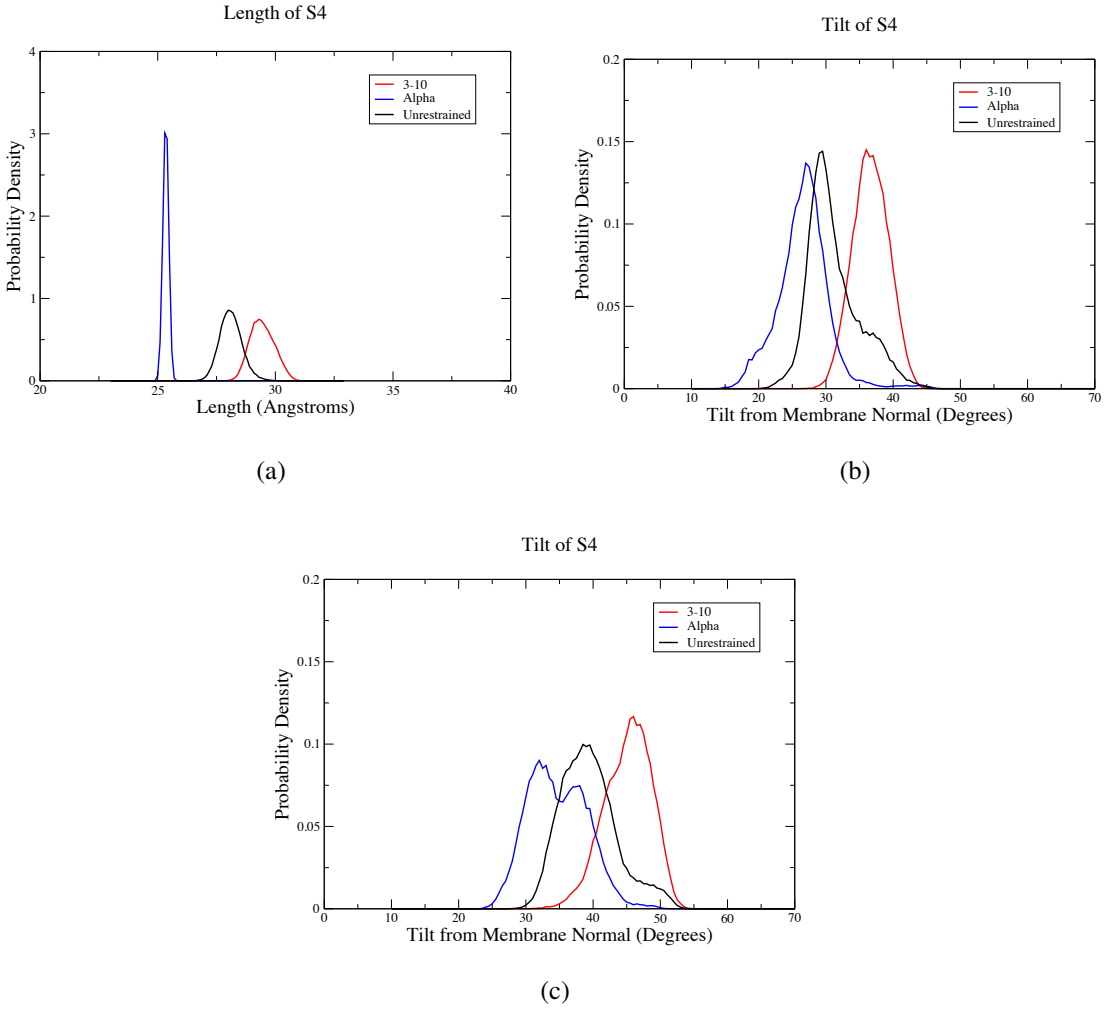

Figure 2.6: : The impact of restraining the S4 helix of the Kv1.2/2.1 chimera to alpha and 3_{10} helical conformations over fully atomistic 100 ns molecular dynamics simulations. a) The length of S4 is dependent upon the secondary structure content of the helix. b-c) The tilt angle of S4 relative to the membrane normal for the 3_{10}, alpha and unrestrained conformations in DPPC (b) and DLPE (c).

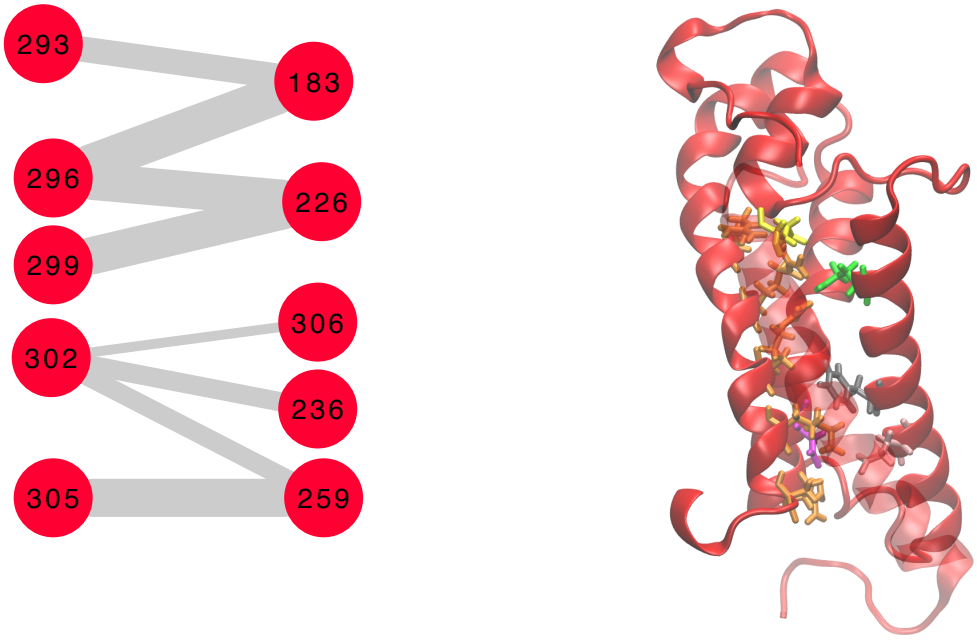

(a) (b)

Figure 2.7: a) The salt bridges between the S4 basic residues (R293, R296, R299, K302, R305) in the 3_{10} simulation that exist in at least 25% of the frames in the simulation. The width of the line is weighted by the frequency of the interaction. b). The final configuration of the voltage sensor in the 3_{10} simulation. Orange: R293, R296, R299, K302, R305. Yellow: E183. Green: E226. Grey: F233. Pink: E236. Magenta: D259.

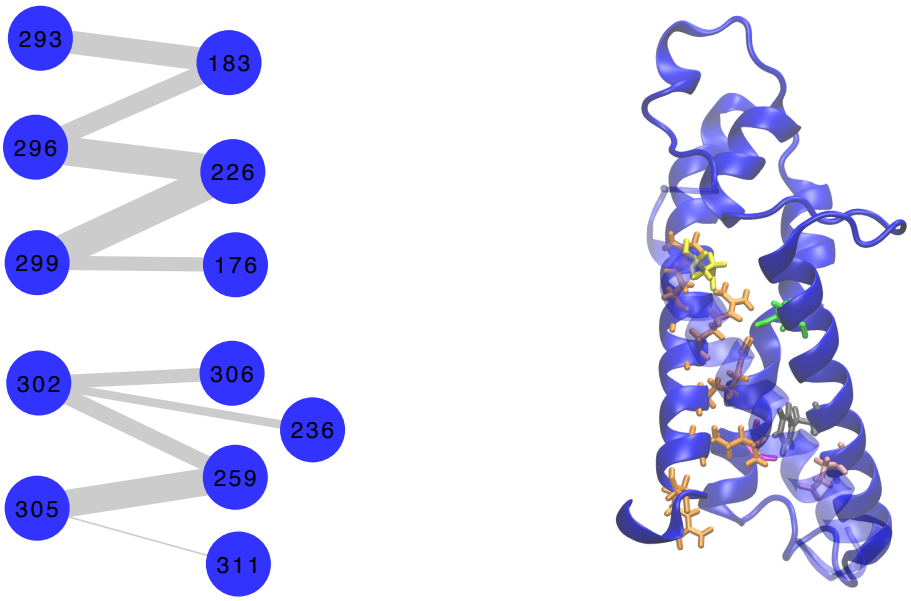

(a) (b)

Figure 2.8: a) The salt bridges between the S4 basic residues in the alpha simulation. The width of the line is weighted by the frequency of the interaction. b). The final configuration of the voltage sensor in the alpha simulation. Residue colors are identical to those in Fig. 2.7.

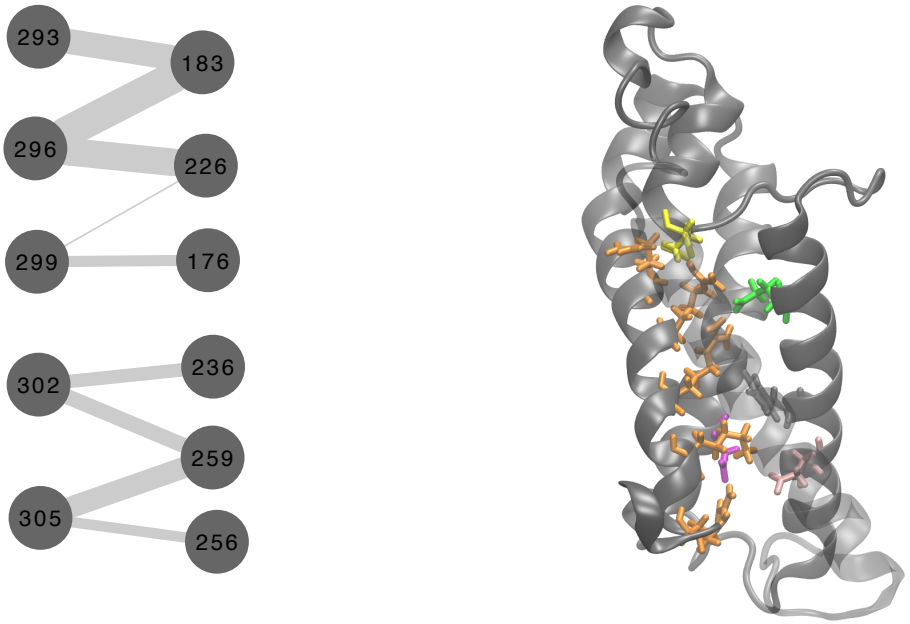

(a) (b)

Figure 2.9: a) The salt bridges between the S4 basic residues in the wildtype simulation. The width of the line is weighted by the frequency of the interaction. b). The final configuration of the voltage sensor in the wildtype simulation. Residue colors are identical to those in Fig. 2.7 and 2.8.

2.4 Discussion

Could, then, the interconversion between alpha and 3_{10} conformations of the S4 helix drive the gating process of Kv channels? Within the voltage sensor, an intrinsic rotation of residues around the axis of S4 takes place as the backbone hydrogen bonding pattern rearranges from i→i+4 to i→i+3, accounting for known experimental data of arginine rotation (reviewed in Tombola et al., 2006). A 3_{10} to alpha interconversion could also facilitate structural modifications beyond the voltage sensor. Tethered to the C-terminal end of the S4 voltage sensing helix, the S4-S5 linker lies in the membrane plane adjacent to the pore gate. Responsible for electromechanical coupling of the voltage sensor to the pore domain, the S4-S5 linker must move 4 Å during the gating process (Haddad and Blunck, 2011; Faure et al., 2012). The elongation and tilt of S4 as it undergoes a change from 3_{10} to alpha results in a lateral displacement of its tail by 4 to 8 Å, depending on if the pivot point is in the middle or edge of the membrane, respectively (Fig. 2.8). The range of lateral motion created by the change in S4 tilt angle would be sufficient to move the linker its known distance during the gating process.

The energetic ramifications of a 3_{10} to alpha helical conversion in S4 could also contribute to the gating process of Kv channels. Given their inherent bistable nature and propensity to open at voltages below 0 mV (Haddad and Blunck, 2011), the open conformation may represent the global energetic minimum of Kv channels, with energy from a hyperpolarizing

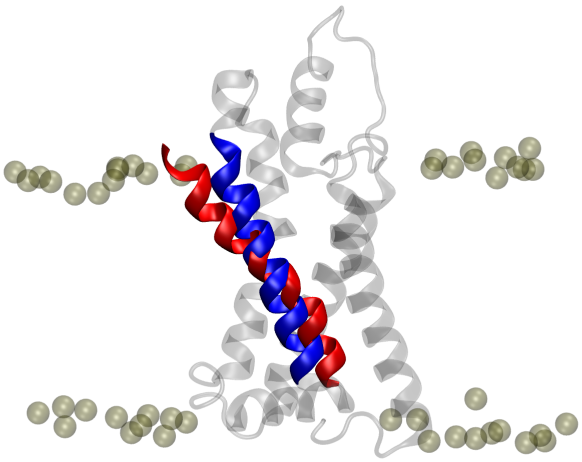

(a)

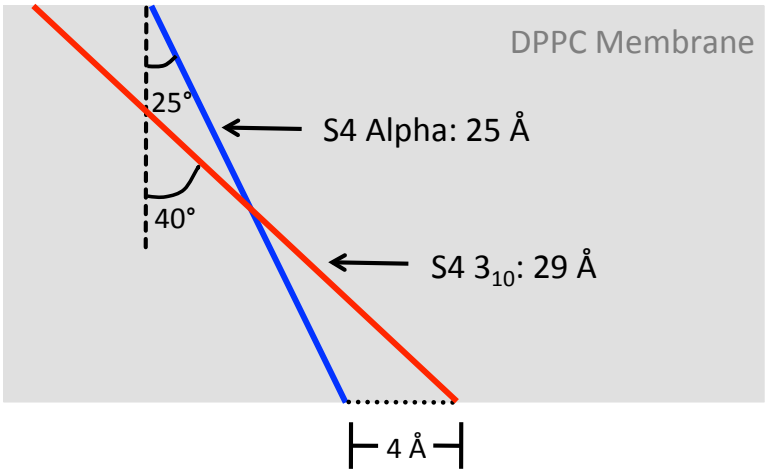

(b)

Figure 2.10: Driven by a hydrophobic mismatch, the elongation of the S4 helix in a 3_{10} conformation tilts away from the membrane normal when compared to the alpha helical conformation. a). The Kv1.2/2.1 chimera S4 helix in alpha (blue) and 3_{10} (red) conformations, superposed along the transmembrane regions of the S1-S3 helices. The yellow balls represent the membrane phosphate groups, delimiting the membrane interior from the aqueous solvent. b) Our simulations reveal that the 3_{10} helix (red) is 4.5 Ångströms longer than the alpha helix (blue) and tilts 15° away from the membrane normal than the alpha conformation. With a pivot point anchored at the center of the S4 helix, an interconversion from alpha to 3_{10} results in a roughly 4 Å translation along the XY plane, in agreement with experimental evidence of S4-S5 linker translocation (discussed further in chapter 3).

voltage contributing to the overall stabilization of the closed state. Given that three to four elementary charges per voltage sensor are displaced under cell polarization (Chanda et al., 2005), a voltage sensor would accumulate about 6 kcal/mol at a resting potential of -70 mV. If the gate is to open without requiring a positive voltage to be applied, that energy needs to be stored in the structure and released under cell depolarization. A 3_{10} helix conformation, which is thought to be intrinsically less stable than the alpha conformation, could provide such energy storage (Yarov-Yarovoy et al., 2012). However, the relative paucity of long (eight or more residues) 3_{10} helices in the Protein Data Bank (Fig. 2.3) has given way to significant discussion about their energetics. A lack of solid data has led to vast differences in the dihedral energetics of 3_{10} helices in different force fields (Patapati and Glykos, 2011). Short simulations of an unrestrained Kv1.2/2.1 chimera voltage sensor with the CHARMM27 (MacKerell et al., 1998) and AMBER-99 (Wang et al., 2000) force fields reveals a significant disparity in the proportion of 3_{10} helix found in S4 between the two force fields (Fig. 2.9). As a result, the choice of force field used in molecular dynamics simulations of Kv channels could result in vastly different conformational changes within both the voltage sensor and, consequently, the pore domain. Recent ultra-long timescale MD simulations have produced a gating transition pathway (Jensen et al., 2012) in the Kv1.2/2.1 chimera. This work relies on the CHARMM27 force field, which heavily favors the alpha helix over the 3_{10} helix conformation (Patapati and Glykos, 2011). Such bias for the alpha helix is likely to manifest itself in these simulations of the Kv channel, thereby

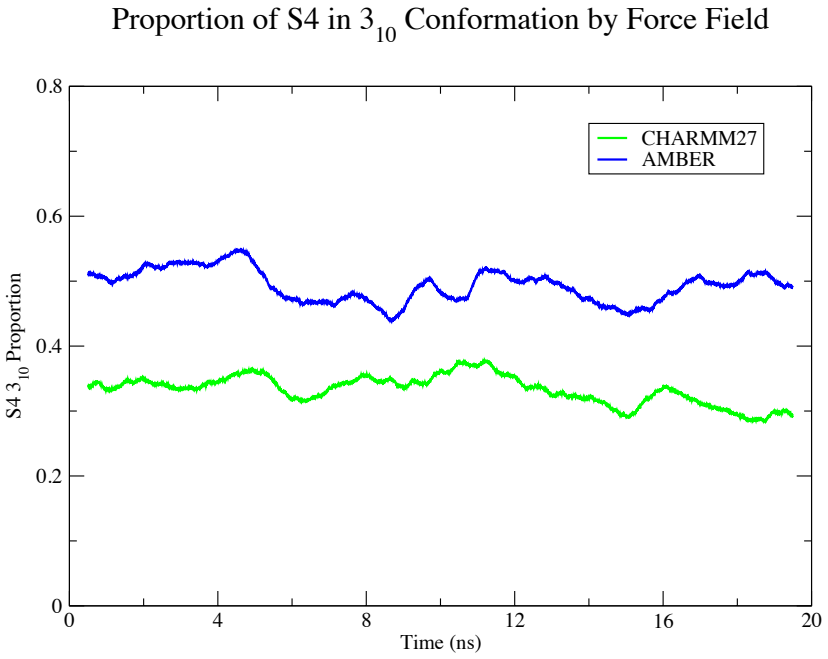

Figure 2.11: The force field used for molecular dynamics simulations influences the 3_{10} helical content of the S4 helix in Kv channels. Above, a running average of 3_{10} helical content in the S4 helix of the Kv1.2/2.1 chimera is calculated from simulations using the CHARMM27 (green) and AMBER-99 (blue) force fields. The difference in 3_{10} helical content between the CHARMM27 and AMBER-99 force fields amounts to roughly one turn (3 residues) of the S4 helix.

neglecting the sampling of any pathways involving interconversion between alpha and 3_{10} helical conformations of the S4 helix. Such discrepancy of the 3_{10} helical content of S4 could ultimately bias the gating transition pathway sampled by molecular simulations.

Understanding the role played by 3_{10} motifs within the S4 helix of voltage sensors will require force fields that better describe the energetics of helical secondary structure. Such empirical force fields can only arise from greater computational and experimental scrutiny

of the 3_{10} helix. A voltage driven modification of the secondary structure of S4 from an alpha to 3_{10} conformation could constitute a simple but effective solution to a complex problem.

Chapter 3

Towards an Atomistic Model of the Closed Conformation of the Kv1.2/2.1 Chimera

3.1 Introduction

Membrane proteins are an integral portion of the proteome in all kingdoms of living organisms, housing photosynthetic reaction centers in autotrophic bacteria, coordinating nutrient uptake and waste expulsion in plants, and maintaining ionic potentials in animals, among

a wide variety of other physiological roles. In fact, membrane proteins are believed to account for roughly one quarter of all proteins in most organisms (Carpenter et al., 2008). Given their essential role in biological processes and their superficial cellular environment, membrane proteins comprise nearly half of all current pharmaceutical targets (Carpenter et al., 2008).

Although membrane proteins are both ubiquitous and extremely valuable pharmaceutical targets, relatively few structures are known. As of December 28, 2013, of the 89,521 protein structures in the Protein Data Bank (Berman et al., 2013), only 1363 structures belong to membrane proteins (White, 2013). Situated within and often spanning both sides of the membrane into the aqueous cellular and extracellular environments, membrane proteins inherently present unique surface electrostatic characteristics (Fig. 3.1). While water soluble proteins more readily form crystals capable of X-ray diffraction, membrane proteins require a more nuanced approach to compensate for the protein's native hydrophobic lipid environment (Caffrey, 2003).

Unsurprisingly, only three structures of Kv channels have been solved (Jiang et al., 2003; Long et al., 2005b, 2007), all of which are in the open conformation. The first crystal structure of a Kv channel, KvAP, seemingly brought more questions to the field than answers (Cohen et al., 2003). With its voltage sensors splayed between the S2 and S3 helices, positioned along the intracellular membrane interface, and oriented away from the pore

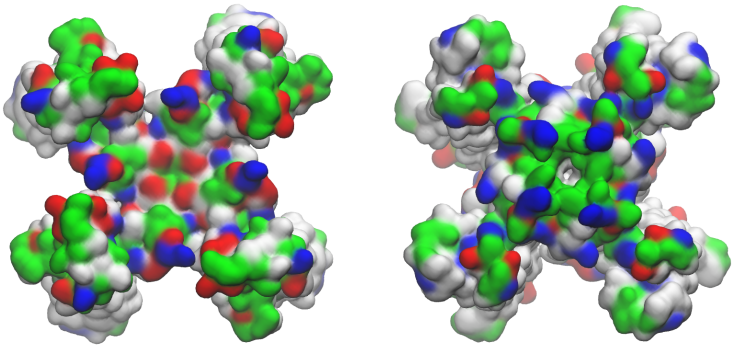

(a) (b)

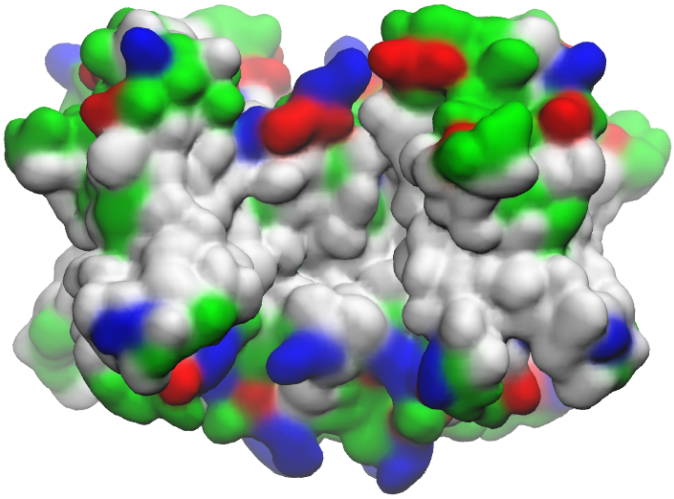

(c)

Figure 3.1: Surface representations of the Kv1.2/2.1 chimera channel shown from the a) top, b) bottom, and c) side, colored according to residue type. Basic residues are shown in blue, acidic residues are shown in red, polar residues are shown in green, and hydrophobic residues are shown in white. The cytosolic faces of the channel (the top (a) and bottom (b)) are highly hydrophilic, reflecting the nature of the aqueous solvent. The lateral faces of the channel, however, are highly hydrophobic as they interface with the hydrocarbon core of the lipid bilayer.

of the channel, both the structure and the mechanism of gating of KvAP and other Kv channels became a highly contentious subject (Swartz, 2004). A variety of biophysical, biochemical, and molecular biology techniques were employed to elucidate the activation mechanism in Kv channels. Though mutagenesis studies, electrophysiology, fluorescent resonance energy transfer, and a variety of other techniques have revealed a host of valuable structural and functional information about the activation of Kv channels (reviewed in Tombola et al., 2006), these methods lack the fully atomic resolution attainable through molecular dynamics simulations.

Molecular dynamics simulations offer unique insights into the behaviors of Kv channels. With a gating time in the tens or hundreds of microseconds, the transition from the open crystal structure to the closed state has been beyond the reach of current molecular dynamics capabilities. To overcome the limitations of the computational burden inherent in Kv channel gating simulations, a number of computational techniques, in concert with experimental evidence, have been used to approach the resting state of both the (S1-S4 monomeric) voltage sensor (Vargas et al., 2011) and the complete (S1-S6 tetrameric) closed channel (Vargas et al., 2012).

While all other molecular dynamics simulations have relied on artificial forces to accelerate the transition between open and closed states, recent advancements in super high performance computing have allowed researchers to sample a pathway between the open

Kv1.2/2.1 chimera channel and a non-conducting state using only an applied hyperpolarizing transmembrane voltage (Jensen et al., 2012). As discussed in Chapter Two, however, the force field used may influence the transition pathway sampled by the channel.

First, in this chapter I will use molecular dynamics to model the voltage sensor in 3_{10} and alpha helical conformations and analyze the effect of a secondary structural transition on the entire channel, including the gate of the pore domain. Then, in collaboration with an experimental group, I will use molecular dynamics simulations to generate a model of the Kv1.2/2.1 chimera in a closed conformation based on luminescence resonance energy transfer (LRET) measurements. The resulting model is the first model of a Kv channel generated from cytosolic measurements (Faure et al., 2012).

3.2 S4 The Effects of a Secondary Structural Transition of the S4 helix on the Kv1.2/2.1 Chimera

3.2.1 Methods

3.2.1.1 Kv1.2/2.1 Chimera Simulations

The transmembrane region (residues 153-417) of the Kv1.2/2.1 chimera channel (PDB code 2r9r) was used for the following studies of Kv channels. To generate a unit cell complete with protein embedded in lipid bilayer and solvent, the CHARMM-GUI web service was used. Fully atomistic systems were built using both DPPC (Fig. 3.2) and DLPE lipids, the TIP3P water model, and 150 mM KCl concentration. The systems were briefly equilibrated (450 ps) using CHARMM36 force field (MacKerell et al., 1998).

The simulations were carried out using the NAMD 2.8 software package (Phillips et al., 2005) with the CHARMM 27 force field. All simulations were run at 303.15 K and 1 atm with Langevin dynamics and the Langevin Nosé-Hoover method to control the temperature and pressure, respectively. The SHAKE algorithm was used to model the high frequency oscillations of hydrogen atoms.

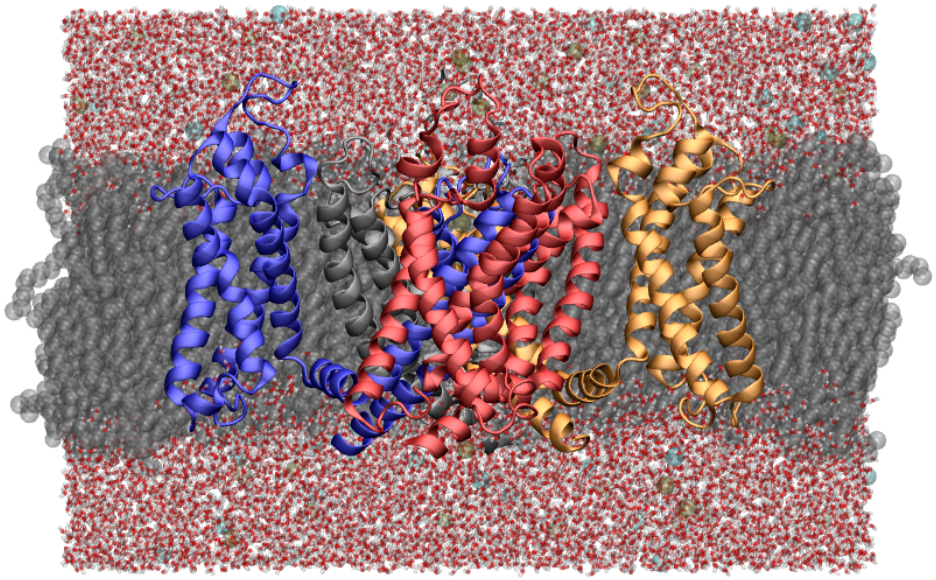

Figure 3.2: The full system used in Kv1.2/2.1 chimera simulations. Pictured above is a DPPC membrane; identical conditions were used in simulations containing a DLPE bilayer.

Table 3.1: Summary of simulations run to test the effect of the secondary structure of S4 on the Kv1.2/2.1 chimera.

SYSTEM	LIPIDS	SIMULATION TIME
3_{10}	DPPC	300 ns
ALPHA	DPPC	300 ns
WILDTYPE	DPPC	200 ns
3_{10}	DLPE	200 ns
ALPHA	DLPE	200 ns
WILDTYPE	DLPE	100 ns

Secondary structure of S4 (residues 285 through 305) was controlled in 3_{10} systems with harmonic restraints of 2.0 Å between the carbonyl oxygens of residue i and the amide hydrogens of residue i+3, as well as harmonic restraints of 3.0 Å between the carbonyl oxygens of residue i and the amide nitrogens of residue i+3. Identical restraints were applied to residues i and i+4 to ensure alpha helicity.

The DPPC simulations were run for 200 ns, while the DLPE systems were run for 100 ns each (Table 3.1). To further describe the differences between the alpha and 3_{10} systems, the 3_{10} and alpha conformations in both lipids were extended for an additional 100 ns (300 ns total in DPPC, 200 ns total in DLPE).

3.2.1.2 Mlotik1 Simulations

Because the Mlotik1 channel was crystallized without its cytosolic cyclic nucleotide binding domain, the entirety of the Mlotik1 crystal structure (PDB code 3BEH) was used for

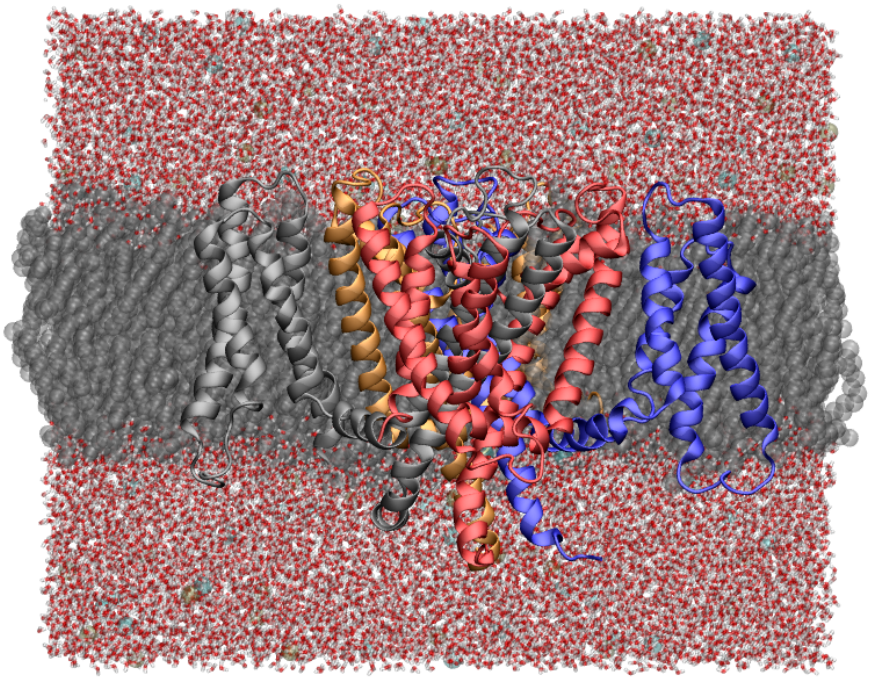

Figure 3.3: The Mlotik1 channel, embedded in a DLPE membrane, after 100 ns of molecular dynamics simulation.

molecular dynamics simulations. An identical protocol was followed as above, though the protein was only simulated in DLPE lipids (Fig. 3.3). The naturally-occurring 3_{10} helix found in the Mlotik1 S4 helix was converted to an alpha helix using identical harmonic restraints discussed above.

3.2.2 Results

Note: given the greater sampling of the DPPC systems, for the following results and discussion sections, the DPPC simulations will be discussed unless otherwise mentioned.

The largest structural changes within the protein occurred within the first 100 ns of simulation. The wildtype system, with no structural modifications imposed, shows the smallest backbone RMSD of the three systems (roughly 3.0 Å). The restraints imposed on the S4 helix did indeed create structural modifications within the protein, both showing higher RMSD values than the unrestrained control system (Fig. 3.4).

Density along the z-axis for protein, water, lipid phosphate and lipid carbonyls were computed and plotted together. These density profiles reveal lipid reorganization between the alpha and 3_{10} systems. In the 3_{10} system, the lipid peaks are broader along the upper leaflet, indicating membrane deformation near the region of structural rearrangement within the protein–the N-terminal end of S4. The lower leaflet, however, produces sharper peaks in the 3_{10} system, possibly due to the stabilizing restraints on the C-terminal 3_{10} helix in the 3_{10} system. The phosphate and carbonyl peaks of both the upper and lower leaflets of the alpha system are much closer to normal distributions than either the wildtype or the 3_{10} system. The shorter alpha helical S4 may be more easily accommodated within the hydrocarbon core of the lipid bilayer, resulting in a more planar bilayer. Given that water density

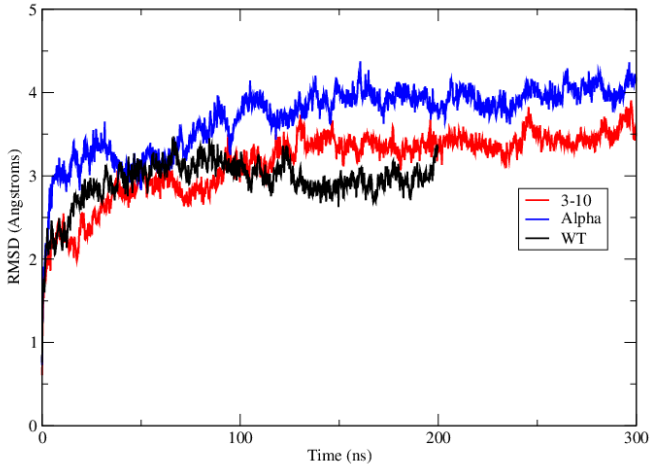

Figure 3.4: Root mean square deviations of the 3_{10}, alpha, and wildtype simulations. RMSD values were calculated along the protein backbone. The reference structures used for the calculations were the post-equilibration coordinates, after S4 restraints had been applied. Consequently, the RMSD differences seen in the 3_{10} and alpha simulations should not reflect the conformational change of the S4 helix.

persists within the core of the bilayer in all three systems, the pores in all three systems are hydrated (Fig. 3.5).

The presence of a pore domain does not affect the tilt angles of the S4 helices when compared to the voltage sensor simulations of Chapter 2. The discrepancy between the tilt angles of the S4 helix in the alpha and 3_{10} systems is roughly 10°, in agreement with the results discussed in Chapter 2.

Very little differentiation can be seen in the centers of mass of the S4 helices in the 3_{10}, alpha, and wildtype systems (Fig. 3.7). A small shoulder on the alpha distribution at 6 Å indicates subunits with a propensity to visit configurations with slightly higher centers of mass.

The salt bridges of the S4 basic residues are largely unaffected by the rearrangement of the secondary structure (Figs. 3.8, 3.9, 3.10). Though the robustness of each interaction varies from system to system, there are two main clusters in each voltage sensor: salt bridges above the "hydrophobic plug" around residue F233, and salt bridges below the hydrophobic plug. With no appreciable rigid body vertical translocation of S4 (Fig 3.7), the hydrogen bond partners of the voltage-sensitive basic residues of S4 are limited.

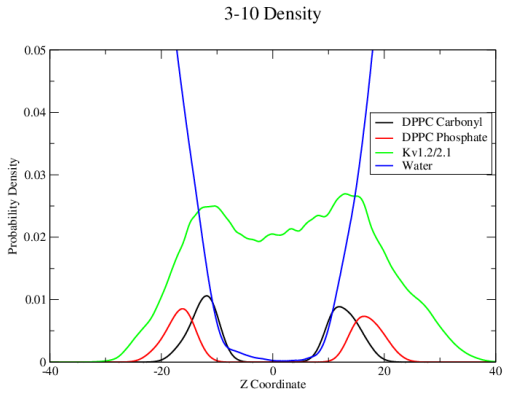

(a)

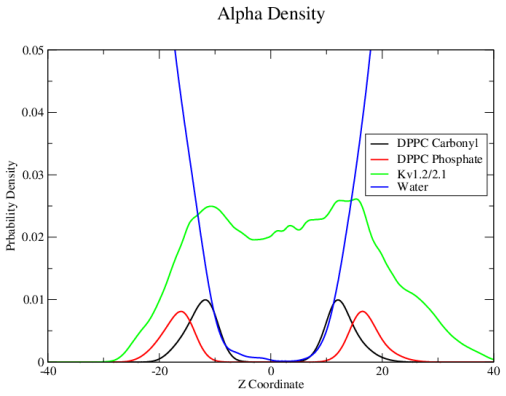

(b)

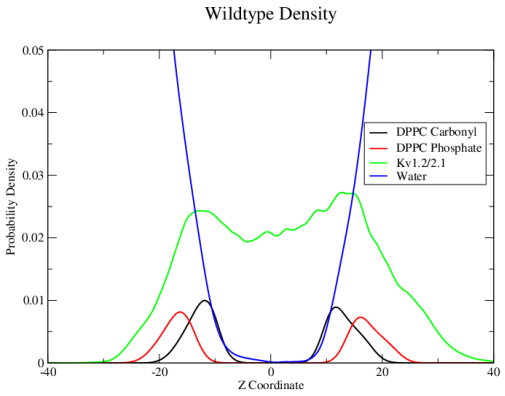

(c)

Figure 3.5: Density profiles of lipid (carbonyls represented in black and phosphates represented in red), water (blue) and protein (green) for the 3_{10}, alpha, and wildtype systems in DPPC membrane.

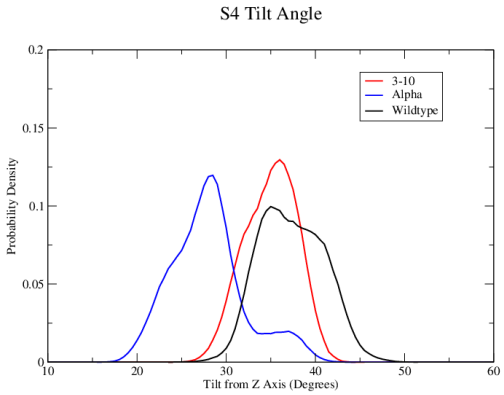

Figure 3.6: Tilt angles of the S4 helices in the Kv1.2/2.1 chimera. Driven by hydrophobic mismatch, the longer 3_{10} and wildtype helices tilt approximately 10° further from the membrane normal than the alpha conformation.

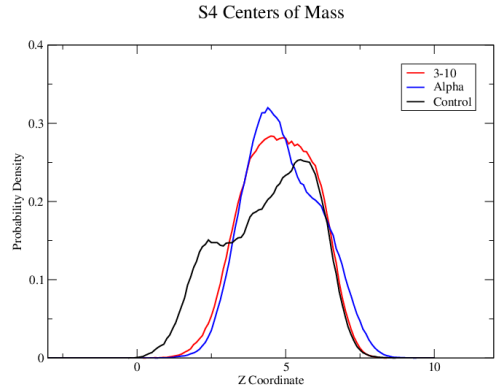

Figure 3.7: The centers of mass of the S4 helices in the Kv1.2/2.1 chimera are unaffected by conformational changes within the S4 helix.

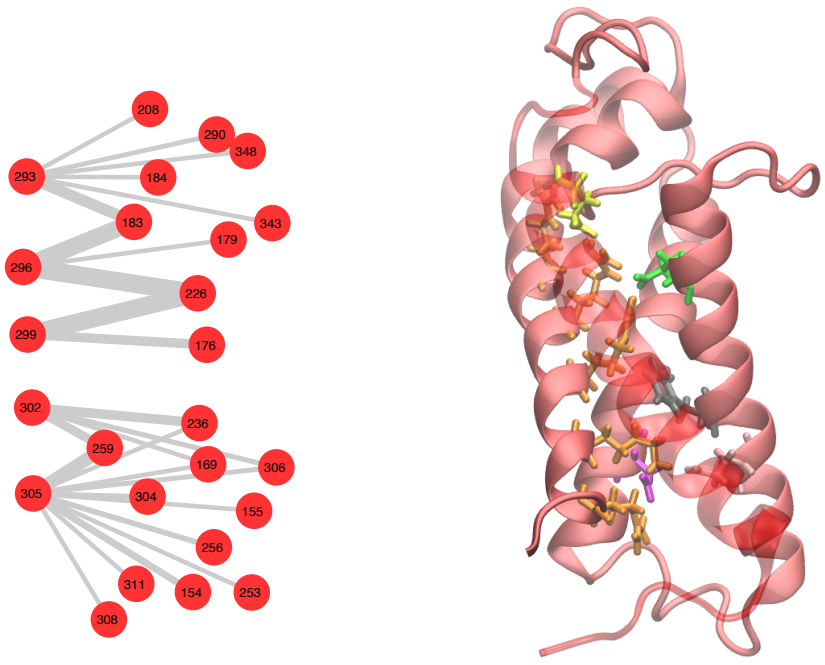

(a) (b)

Figure 3.8: a) The salt bridges between the S4 basic residues (R293, R296, R299, K302, R305) in the 3_{10} simulation. The width of the line is weighted by the frequency of the interaction. b). The final configuration of the voltage sensor in the 3_{10} simulation. Orange: R293, R296, R299, K302, R305. Yellow: E183. Green: E226. Grey: F233. Pink: E236. Magenta: D259.

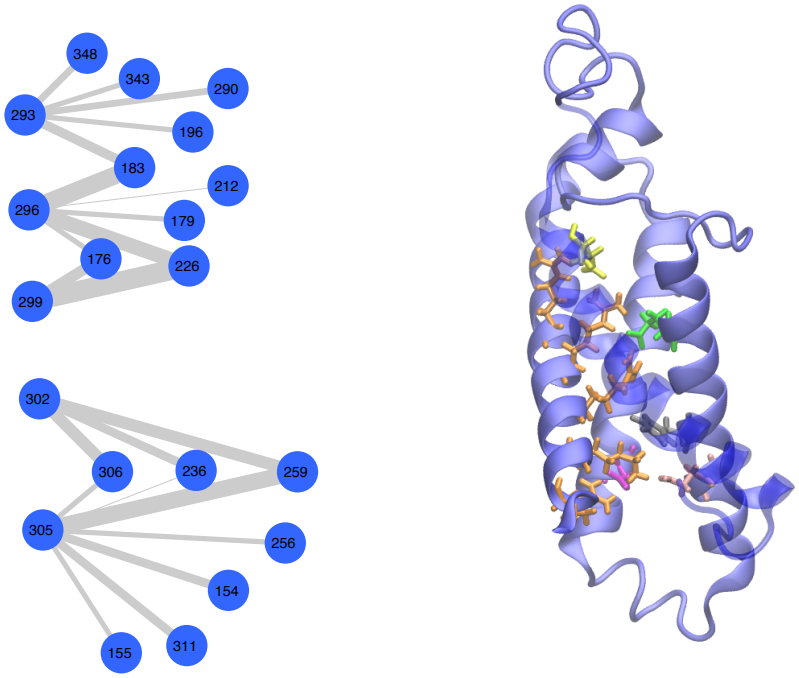

(a) (b)

Figure 3.9: a) The salt bridges between the S4 basic residues in the alpha simulation. The width of the line is weighted by the frequency of the interaction. b). The final configuration of the voltage sensor in the alpha simulation. Residue colors are identical to those in Fig. 3.8.

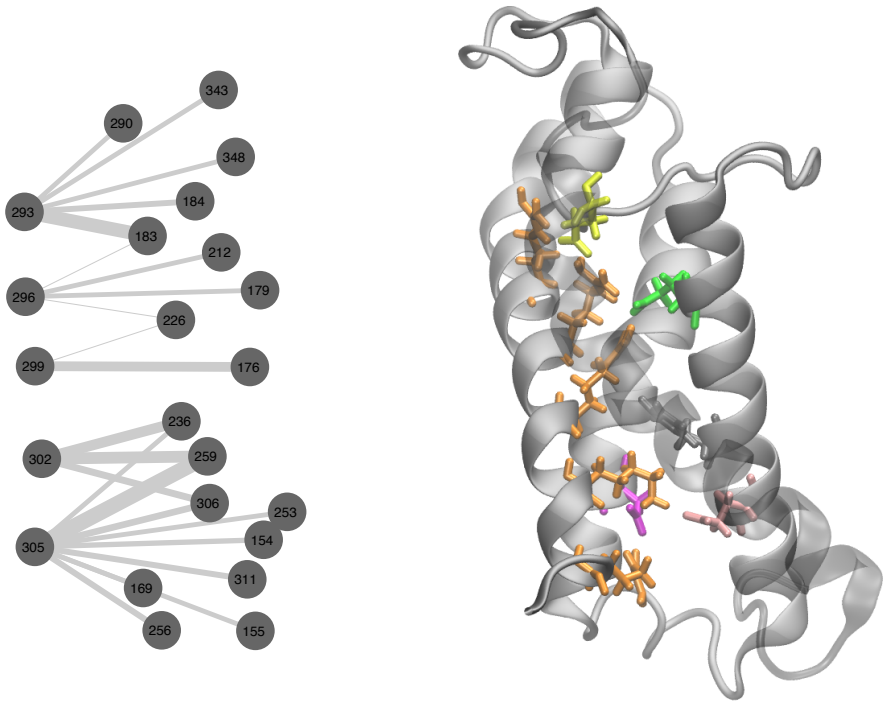

(a) (b)

Figure 3.10: a) The salt bridges between the S4 basic residues in the wildtype simulation. The width of the line is weighted by the frequency of the interaction. b). The final configuration of the voltage sensor in the wildtype simulation. Residue colors are identical to those in Fig. 3.8 and 3.9.

3.3 A Molecular Mechanics Model of a Closed Voltage-Gated Potassium Channel Generated from S4-S5 Linker LRET Measurements

3.3.1 Introduction

Existing models of the closed state of Kv channels have relied mainly on measurements from the extracellular side of the channel (Lainé et al., 2003; Campos et al., 2007; Lin et al., 2010) and from measurements from within the voltage sensor (Henrion et al., 2012). Though the voltage sensor is the primary actor in the gating process, it naturally follows that its structural modifications must somehow be transferred to the pore domain. The S4-S5 linker, an amphipathic helix traversing the XY plane, connects the C-terminal end of the S4 helix with the N-terminal end of the pore domain–the S5 helix (Fig. 3.11). To quantify the conformational changes that occur on the cytosolic face of the channel, the Rickard Blunck laboratory, our experimental collaborators at the University of Montreal, varied the lipid composition to shift the channel equilibrium between open and closed conformations (Xu et al., 2008). The Blunck laboratory then performed luminescence resonance energy

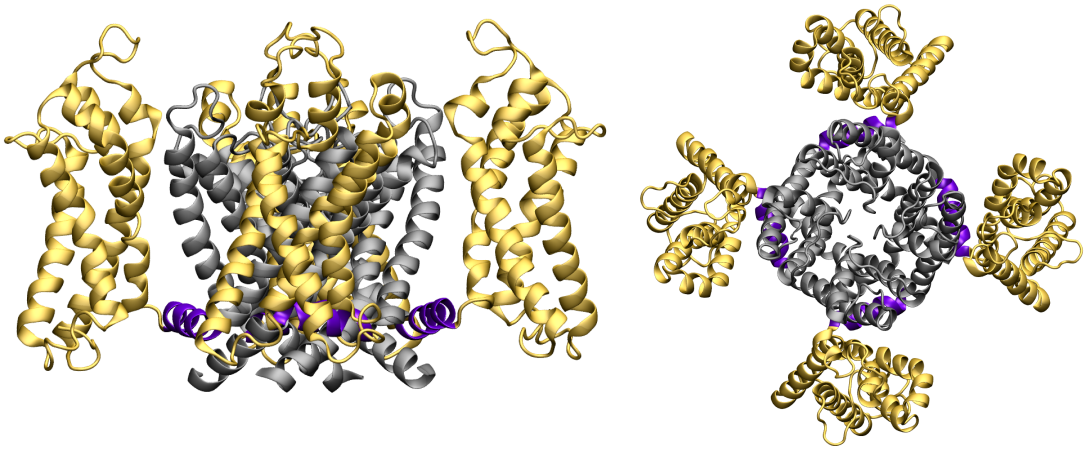

Figure 3.11: The S4-S5 helix (purple), connecting the voltage sensor (yellow) to the pore domain (black), is the site of electromechanical coupling in Kv channels.

transfer (LRET) experiments to quantify cross-pore distances of atoms along the S4-S5 linker in both the open and closed conformations.

To model the full channel in the closed conformation, the LRET recordings along the S4-S5 linker were used as restraints from molecular dynamics simulations of the Kv1.2/2.1 chimera. The simulations reveal that, indeed, the pore of the channel is closed, and that a small 3-4 Å radial motion of the S4-S5 linker is sufficient for channel gating. In the closed conformation, structural features agree with previously reported values (Faure et al., 2012). In the discussion of Chapter 3, I will compare the closed model generated with the model generated from S4 restraints alone.

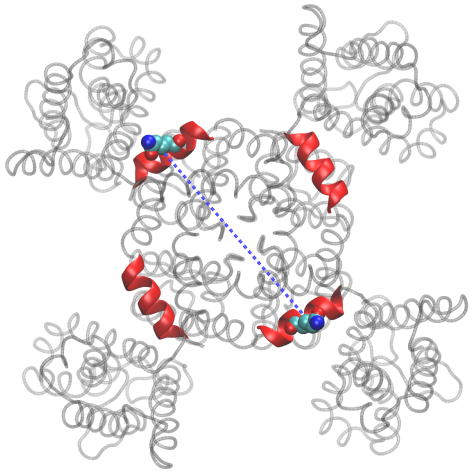

Figure 3.12: A cross-pore restraint mimicking the distance measurements recorded from LRET experiments. The S4-S5 linker is shown in red. Here, a blue dashed line is used to represent the harmonic distance restraint between C gamma atoms of residue 315Q.

3.3.2 Methods

The Kv1.2/2.1 chimera structure (Protein Data Bank (PDB) code 2R9R) was used as a template for model generation. Using the CHARMM27 force field for proteins (MacKerell et al., 1998), the initial structure was placed in a generalized Born implicit solvent membrane model (Im et al., 2003), minimized, and briefly simulated (50 ps) with flat-bottomed harmonic restraints of 10 kcal/mol to mimic the experimental results of the Blunck group (Table 3.2, Figure 3.12).

The resulting "closed" structure was then reconstituted into DPPC bilayers using the CHARMM-GUI web service (Jo et al., 2008) and equilibrated by gradually releasing protein backbone restraints over 450 ps. A potential of −500 mV was applied to the closed

Table 3.2: Atomic distances for the S4-S5 linker in the closed conformations (as measured by LRET) and the Kv1.2/2.1 chimera crystal structure.

Atom ID	Closed	Kv1.2/2.1 Crystal
G313C	33.4 ± 2.7	42.9
L314C	42.8 ± 0.9	49.8
Q315C	40.2 ± 0.4	52.4
I316C	30.1 ± 0.5	38.0
G318C	37.9 ± 1.5	48.3
Q319C	33.2 ± 1.1	39.8
K322C	35.9 ± 0.3	44.4

system with NAMD 2.8 (Phillips et al., 2005) and the CHARMM27 and CHARMM36 (Brooks et al., 2009) force fields for proteins and lipids, respectively. The system was simulated for 100 ns with harmonic restraints applied to linker atoms throughout. Temperature was held constant at 303.15 K with Langevin dyanmics, and pressure was held constant using the Langevin Nosé-Hoover method. Water was represented with the TIP3P water model, and high frequency hydrogen vibrations were constrained with the SHAKE algorithm. Aspartate, glutamate, and arginine residues were reparameterized to recently published values (Jensen et al., 2012). Additional harmonic restraints between the α-carbons of Ile-230 and Tyr-267, Ile-230 and Arg-290, and Ile-177 and Arg-290 were added to the closed system in accordance with previously published work (Campos et al., 2007; Lin et al., 2010).

To create a final model of the closed state, one subunit from the closed simulation was used to create a four-fold symmetric model. This tetramer was reinserted in a generalized born implicit membrane and minimized with flat-bottomed harmonic restraints of 50 kcal/mol on the linker atoms, as well as lighter harmonic restraints of 10 kcal/mol along the linker backbone to promote helicity. The protein was again reconstituted into a DPPC bilayer, solvated with TIP3 water molecules, and re-equilibrated with 10 kcal/mol backbone helical restraints applied to the linker and the bottom of S4, as well as the aforementioned flat-bottomed 50 kcal/mol harmonic linker restraints in accordance with our luminescence resonance energy transfer (LRET) measurements. The resulting model was simulated for 150 ns, the results of which are reported below.

A similar simulation protocol was used for simulations of the MlotiK1 channel crystal structure (PDB code 3BEH) embedded in a DPPC bilayer. However, no additional restraints were applied to the system, and no amino acid reparameterization was necessary.

3.3.3 Results

With harmonic restraints applied to sidechain carbons, the S4-S5 linker, running transverse to and surrounding the S6 transmembrane gating helices, moves 3-4 Å inward in the closed model relative to control, in agreement with experimental results.

The S4 helix moves significantly downward in the closed model. The center of mass of the S4 helix, which exists at roughly 6 Å in the open crystal conformation, is roughly 4-7 Å lower in the membrane (Fig. 3.13a). The S4 helix also adopts a more vertical orientation within the membrane, tilting toward the Z-axis (Fig. 3.13b).

The S4 helix, without harmonic potentials restraining its secondary structure, is free to evolve into its energetic minimum. The 3_{10} helical propensity, $P_{3_{10}}$, is defined as:

$$P_{3_{10}} = \frac{\int b_t \cdot dt}{(r-3) \cdot T} \times 100$$

Where $P_{3_{10}}$= 3_{10} helical propensity, t = time, T = duration of simulation, b_t = number of i$\rightarrow$i+3 hydrogen bonds on the S4 helix at time t, and r = the number of total residues on the helix. In short, the $P_{3_{10}}$can be described as the percentage of the S4 helix in a 3_{10} conformation.

With restraints constraining the S4-S5 linker to its closed position, the S4 helix maintains its C-terminal 3_{10} helix, though it is slightly shorter than the 3_{10} helix found in the Kv1.2/2.1 crystal (Fig. 3.14a). The 3_{10} helix itself, situated lower in the membrane leaflet, distorts slightly (Fig. 3.14b).

With its lower center of mass, the basic voltage sensing residues are able to rearrange their salt bridge configurations. Though the alpha and 3_{10} S4 salt bridge configurations

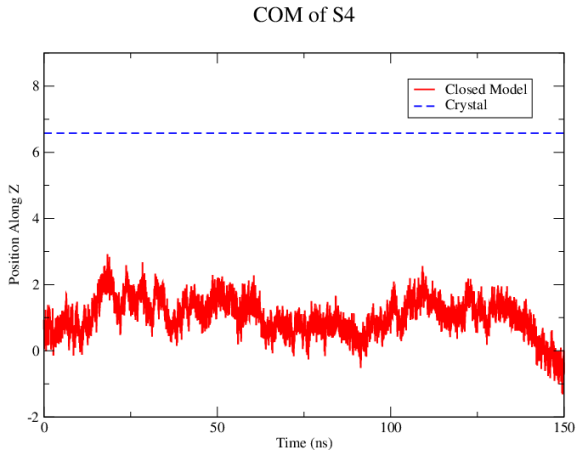

(a)

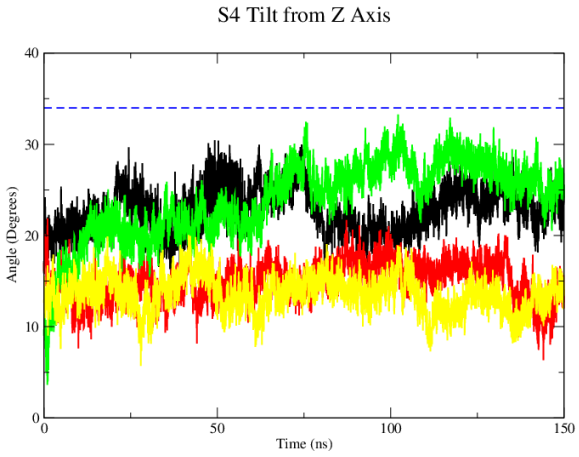

(b)

Figure 3.13: The S4 helix undergoes significant rearrangement in simulations with the S4-S5 linker restrained to its closed position. a). The center of mass of the S4 helix is roughly 6 Å lower than its position in the Kv1.2/2.1 chimera crystal structure (blue dashed line). b). The tilt angles of each subunit of the Kv1.2/2.1 chimera throughout the simulation. The S4 helices tilt toward the pore domain when compared to the open crystal structure (blue dashed line).

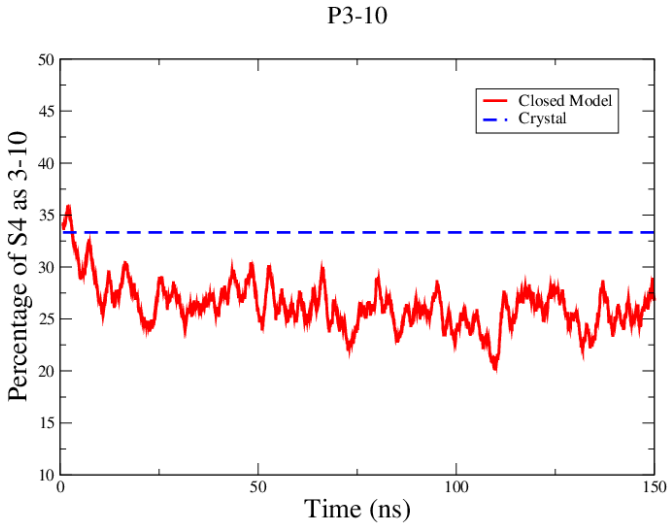

(a)

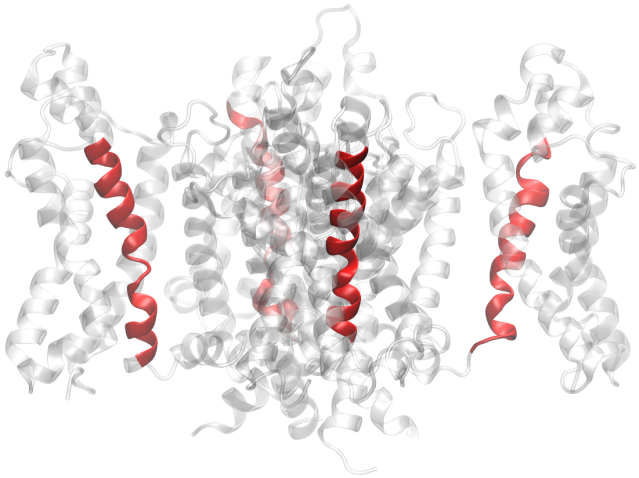

(b)

Figure 3.14: The 3_{10} helix in S4 persists with the S4-S5 linker restrained to its closed conformation, as determined by LRET distance measurements imposed as harmonic distance restraints in MD simulations. a) The 3_{10} helical propensity of the S4 helix over 150 ns simulations with the linker in its closed configuration. b). The S4 helix (red), though lower in the membrane, distorts slightly in the region of the voltage sensor "hydrophobic plug."

were largely similar, the closed linker configuration with voltage sensor restraints induced a downward motion of the S4 helix. Subsequently, the basic arginines and lysine of S4 moved downward roughly one turn. R4 translated below the hydrophobic plug centered near F233 (Lacroix and Bezanilla, 2011), interacting with E236 near the inner leaflet (Fig. 3.15).

3.4 Discussion

3.4.1 The Effect of A Secondary Structural Modification of S4 on the Pore Domain

In Chapter 2, molecular dynamics simulations suggested that a simple secondary structure modification of the S4 helix could rectify many seemingly disparate results from biophysical studies of the gating transition of Kv channels. How, then, does the secondary structure of the S4 voltage sensing helix affect pore domain, and, consequently, the conduction of K^+ through Kv channels?

The S6 helices comprise the inner region of the pore domain through which K^+ permeate (Yifrach and MacKinnon, 2002). Believed to open and close in an iris-like motion (Labro and Snyders, 2012), the conformational change of the pore domain must be linked to the

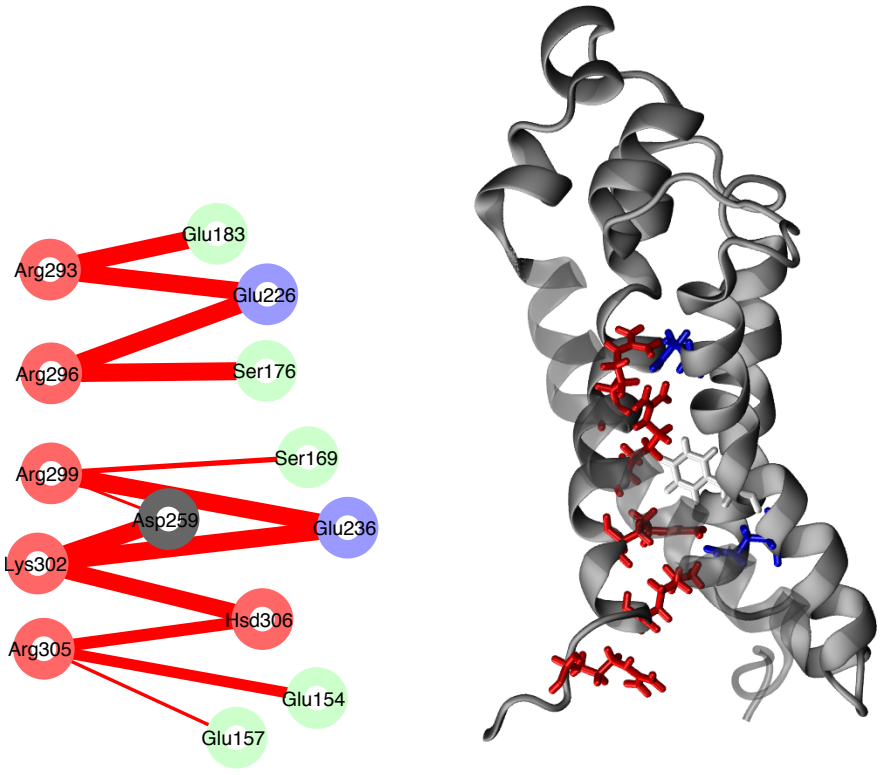

(a) (b)

Figure 3.15: The voltage sensitive basic residues of S4 move "down" in the closed linker simulations. a). The salt bridge interactions of the S4 basic residues (R2, R3, R4, K5, R6). The width of the line indicates the probability of the interaction, calculated from the interaction time of the MD simulations. b). The resulting voltage sensor configuration. The S4 basic residues are shown in red; E226 and E236 are shown in blue; F233 is shown in white.

voltage sensing domain to regulate the conductance of the channel. Consequently, the radius of the pore domain can serve as a metric to demarcate the state of the channel. A narrow pore radius signifies a closed, nonconducting channel, whereas a wider pore radius is more likely to conduct K^+.

To quantify the pore opening and closing in the aforementioned simulations, the Hole software package was used to calculate the pore radius over the final 100 nanoseconds each simulation (Fig. 3.16a-c). In short, a secondary structural modification of the Kv1.2/2.1 chimera S4 helix was insufficient to influence the state of the gate in the pore domain of the channel.

Unlike the existing structures of voltage gated K^+ channels, the transmembrane region of MlotiK1, a 6 TM cyclic nucleotide gated K^+ channel, is crystalized in the closed conformation. Intriguingly, its S4 helix adopts a 3_{10} helix spanning the entire transmembrane region. Because the gating of MlotiK1 is triggered by the binding of a cyclic nucleotide to an intracellular domain on the channel, the S4 helix does not contain the highly-conserved basic residues found on voltage gated K^+ channels. This S4 secondary structural similarity arising from a highly divergent primary amino acid sequence suggests a structural role for the 3_{10} helix found on S4. As in the Kv1.2/2.1 chimera simulations, the state of the gate of the pore domain was largely unaffected by a conformational change of the S4 helix (Fig. 3.17).

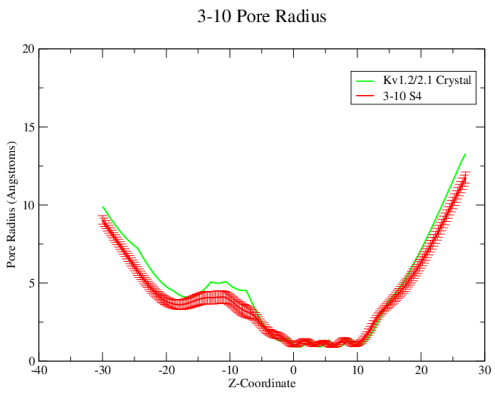

(a)

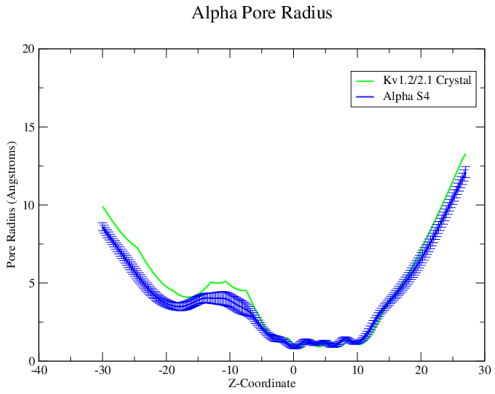

(b)

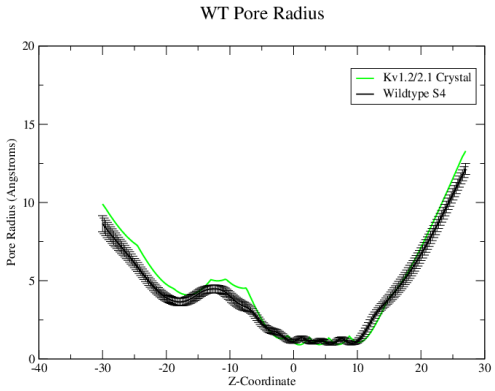

(c)

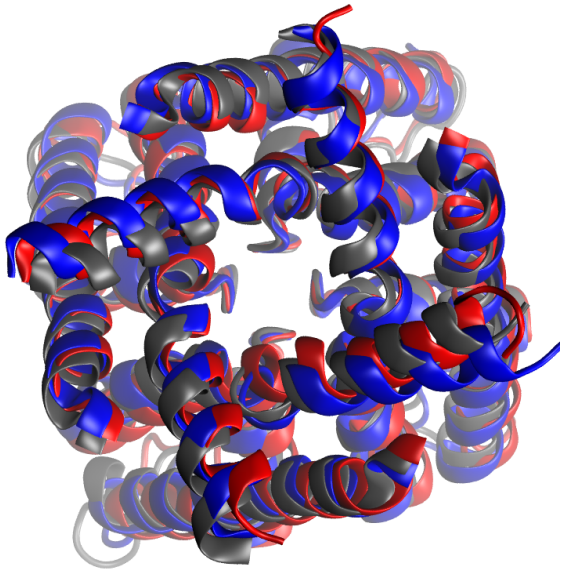

(d)

Figure 3.16: An alpha to 3_{10} helical interconversion of the S4 helix has little effect on the S6 gating helices of the Kv1.2/2.1 chimera pore domain. a-c) The average pore radii of the final 100 ns of simulation for the 3_{10}, alpha, and wildtype systems. d). The final configurations of the pore domains of the 3_{10} (red), alpha (blue) and wildtype (grey) simulations as viewed from the cytosolic face of the channel.

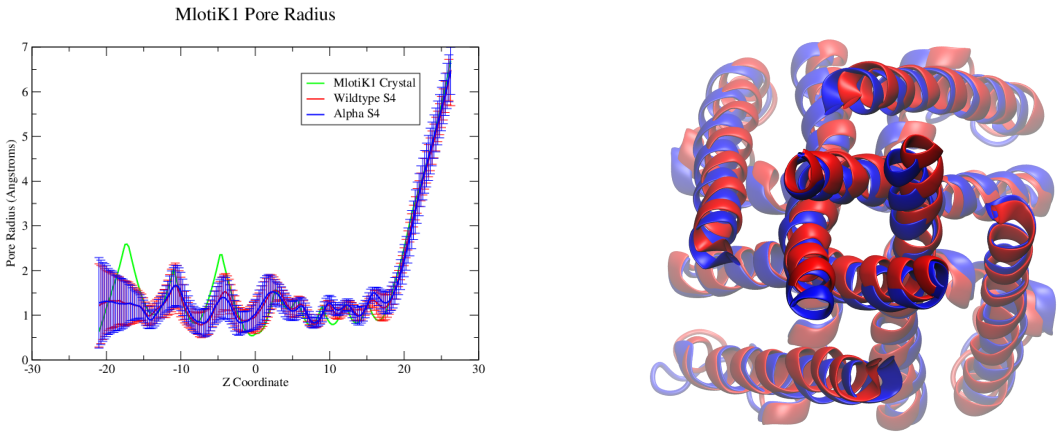

(a) (b)

Figure 3.17: The pore domain of the MlotiK1 channel is unaffected by a conformational change of the S4 helix. a) The average pore radii of the final 50 ns of simulation for the wildtype (full 3_{10} helical S4, red) and alpha helical S4 (blue) conformations. The pore radius of the closed crystal structure is shown in green for reference. b). The final configurations of the MlotiK1 pore domains in the wildtype (red) and alpha (blue) simulations.

As with all molecular dynamics simulations, the time required for the conformational change to occur may exceed the timescale attainable with current computational resources. At the timescales sampled in the above simulations, an interconversion between alpha and 3_{10} helical conformations of the S4 helix induces neither opening nor closing of the gate in 6 TM K^+ channels.

3.4.2 Modeling the Closed Kv1.2/2.1 Chimera from S4-S5 Linker LRET Measurements

Using luminescence resonance energy transfer measurements of a closed Kv channel as distance restraints along the S4-S5 linker brought about an inward motion of the S6 gating helices, restricting the pore radius and effectively closing the channel in the MD simulations (Fig. 3.18). Employing the same method as in Chapter 3.4.1 to calculate the pore radius, a significant reduction in both the radius and volume of the pore hinders K^+ permeation.

As seen in Figure 3.18c, the closed linker position induces only a slight motion of the S6 helices when compared to the open pore of the crystal structure of the Kv1.2/2.1 chimera. In order to verify that the pore of the closed model had actually closed, the number of water molecules within the pore vestibule was calculated for the closed linker simulation and compared to the wildtype simulation (Fig. 3.19). In the closed model, pore constriction

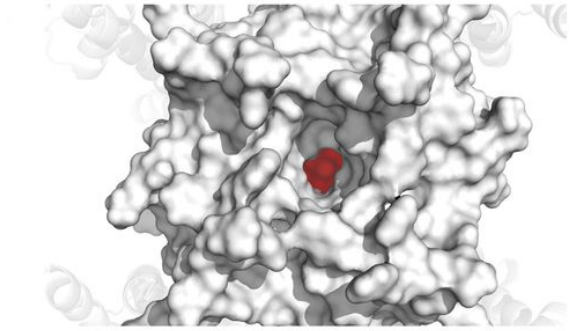

(a)

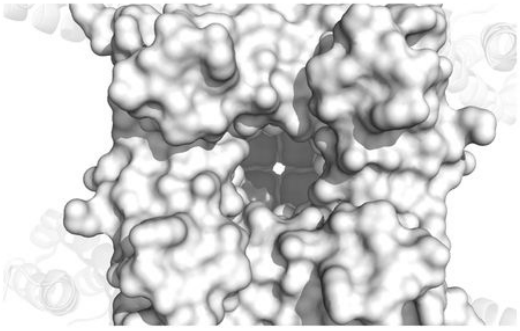

(b)

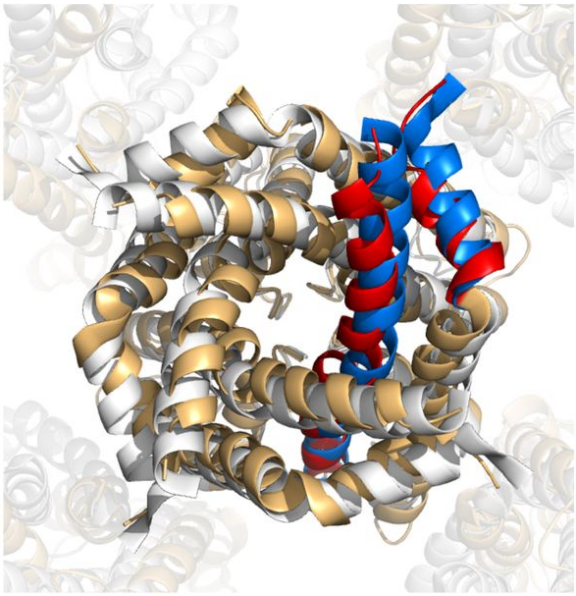

u

(c)

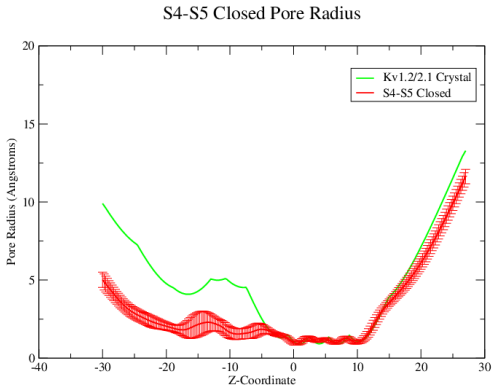

(d)

Figure 3.18: a). The pore domain of the closed model is blocked by the sidechains of I398 in the closed conformation of the channel. b). The selectivity filter of the Kv1.2/2.1 chimera crystal structure is visible from the cytosolic face of the channel, allowing ion permeation through the channel. c) A small 4 Å motion of the S4-S5 linker sufficiently pushes the S6 helix inward in the closed (red) channel from the open (blue) conformation. d). The pore radius of the closed model is significantly more narrow than the crystal structure, preventing K^+ flux through the pore domain.

occurs at residue I398, inhibiting solvent exchange between the cytosol and the channel pore. Thus, a small motion of roughly 4 Å of the S4-S5 linker is sufficient for gating in Kv channels.

Interestingly, the S4 helix of the closed channel adopts a strikingly different orientation than in the crystal structure. Moving as a rigid body, S4 translates roughly 6 Å downward along its own axis. The S1-S4 voltage sensor helical bundle, arranged roughly in an hourglass shape, is divided near the helical constriction point by a bundle of hydrophobic residues, often referred to as the "hydrophobic plug." The downward motion of S4 evident in the simulations facilitates the translocation of R299 across the hydrophobic plug of the voltage sensor. F233, located on the S2 helix and situated within the hydrophobic plug, is believed to be involved in the regulation of S4 translocation, though the mechanism is debated (Tao et al., 2010; Khalili-Araghi et al., 2010; Schwaiger et al., 2013). In the closed model, the hydrophobic plug is maintained, still demarcating the residues of the upper leaflet (R293, R296) from those of the lower leaflet (R299, K302, R305). Though this single residue translocation is modest in comparison with other models (Delemotte et al., 2011; Henrion et al., 2012; Jensen et al., 2012), the overall downward motion of the S4 helix is well within the accepted range of motion of between 6-15 Å (Vargas et al., 2011; Yarov-Yarovoy et al., 2012; Jensen et al., 2012).

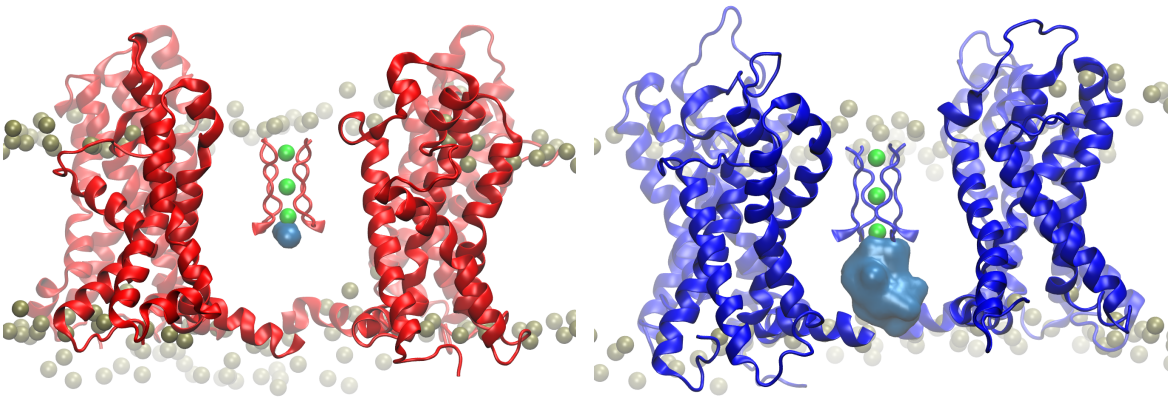

(a) (b)

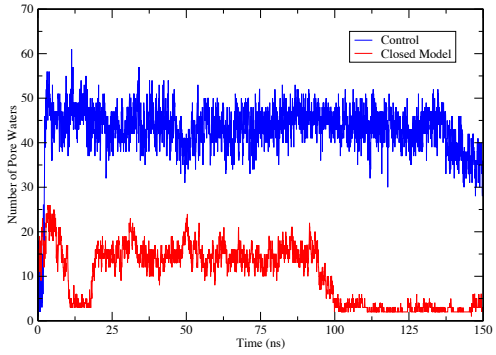

(c)

Figure 3.19: a). An inward motion of 4 Å is sufficient to restrict solvent access in the closed model of the Kv1.2/2.1 chimera. b) The pore of the unrestrained Kv1.2/2.1 chimera is fully hydrated throughout 150 nanoseconds of simulation. c). Solvent is excluded from the closed model of the Kv1.2/2.1 chimera.

The C-terminal 3_{10} helix endures in the closed model, as predicted in other computational studies of the Kv1.2/2.1 chimera (Khalili-Araghi et al., 2010). Additionally, the S4 helix pivots at its C terminus away from the S4-S5 linker in the closed model. In the open structure, the S4 helix and the S4-S5 linker form an acute angle of roughly 67°. In the closed model, however, S4 tilts away from the S4-S5 linker by nearly 45°, creating an angle of 104° between the S4 helix and the S4-S5 linker, in agreement with previously published results predicting an increased tilt of 40° between S4 and the linker (Fig. 3.20) (Yarov-Yarovoy et al., 2012).

But is this model of the closed channel stable? After 100 ns, all restraints on the channel were released and the closed channel was simulated for 50 ns. Completely unrestrained, the pore of the channel remained closed (Fig. 3.21). Thus, using LRET measurements of the S4-S5 linker to complement molecular dynamics, we have found a closed conformation of the Kv1.2/2.1 chimera that not only agrees with previously published data, but also represents a stable conformation of the channel.

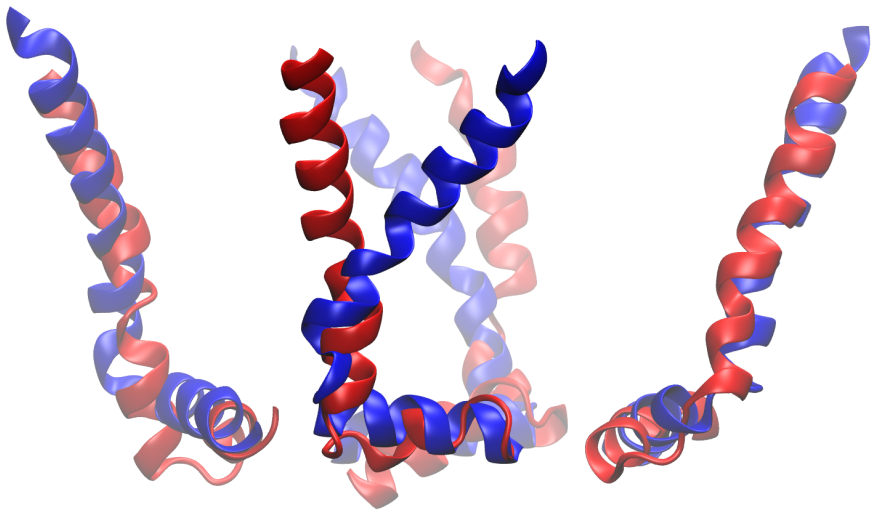

Figure 3.20: The angle between the S4 helix and the S4-S5 linker increases by roughly 40° from the open conformation (blue) and the closed model (red).

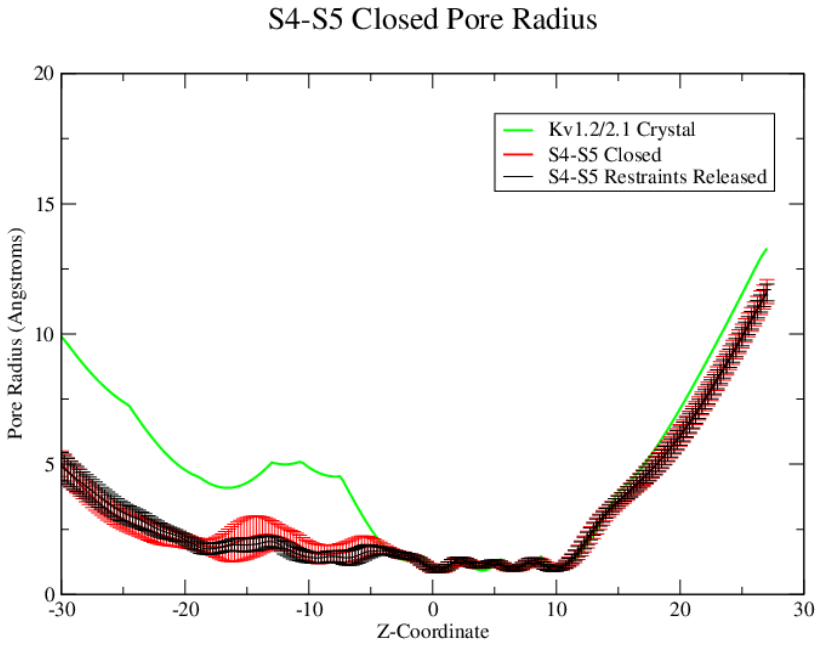

Figure 3.21: The pore of the Kv 1.2/2.1 chimera remains closed when all restraints on the channel are released after 100 ns. For comparison, the pore radii of the open crystal structure (green) and the restrained channel (red) are shown along with the pore radius of the unrestrained closed channel (black).

Chapter 4

The Energetics of Gating the KvAP Channel Pore Domain

4.1 Introduction

To maximize the efficiency of the myriad of chemical reactions driving the cellular processes necessary to sustain life, it is essential to control the environmental conditions around the reaction site. In vivo, the phospholipid bilayer delineates the cytoplasm from its surrounding environment. Composed of hydrophilic phosphate headgroups and a hydrocarbon core, the cell membrane is permeable only to small, nonpolar molecules. Potassium, an

essential ion for many prokaryotic and eukaryotic organisms, cannot traverse the nonpolar cell membrane. Consequently, additional cellular machinery is needed to facilitate nutrient uptake and waste elimination across the lipid membrane.

Potassium ion channels, tetrameric proteins spanning the length of the cell membrane, enable potassium permeation across the cell membrane (Hodgkin and Huxley, 1952). Potassium conduction occurs through the channel's pore domain, comprised of the S5 pore-lining helix and the S6 gating helix. In voltage gated potassium ion channels, the conformation and orientation of the S6 gating helix is coupled to the conformation of the voltage sensor. At the cellular resting potential of roughly -70 mV, the voltage sensor is in its "down" conformation and the S6 helix is closed. As the cell depolarizes from the influx of Na^+ during an action potential, Kv channel voltage sensors move towards their "up" configuration, and the S6 helices move apart, enabling K^+ conductance through the pore domain and out of the cell (Hodgkin and Huxley, 1952; Jiang et al., 2003).

Potassium ion permeation through Kv channels is highly selective. The selectivity filter, creating the extracellular mouth of the protein, uses its backbone carbonyls to coordinate K^+ permeation via a knock-on mechanism (Berneche and Roux, 2001; Zhou et al., 2001). Access to the selectivity filter is regulated by the gate formed by the S6 helices (Fig. 4.1) (Zhou et al., 2001; Jiang et al., 2003; Long et al., 2005b, 2007).

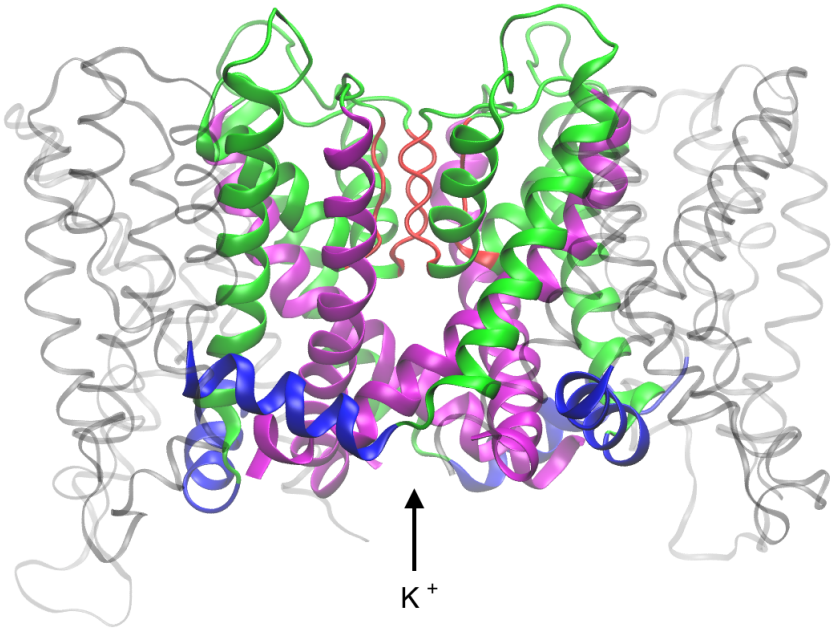

Figure 4.1: The KvAP K+ channel in its open conformation (Schow et al., 2012). Ion permeation occurs from the intracellular side of the channel, between the S6 gating helices (magenta) and through the selectivity filter (red). The S4-S5 linker (blue), responsible for electromechanical coupling, connects the voltage sensing domain (grey) to the pore domain.

Though the energetics of ion permeation through the selectivity filter are well understood (Berneche and Roux, 2001; Wojtas-Niziurski et al., 2013), the energetics of gating the pore domain remain unclear. Mutagenesis studies of the S6 helix suggest that the closed pore domain represents an energetic minimum (Hackos et al., 2002; Yifrach and MacKinnon, 2002), as mutations along S6 destabilize the closed conformation. Recent ultra-long molecular dynamics simulations suggest that the S6 helices are at their energetic minimum when packed together in the closed conformation (Jensen et al., 2012). However, recent free energy calculations of the Kv1.2/2.1 chimera pore domain find the open conformation of the pore domain energetically favorable to its closed configuration (Fowler and Sansom, 2013).

Gating of a Kv channel requires two steps: first, the voltage sensors on the protein's periphery reorganize in response to a change in the transmembrane potential. This reorganization influences the location of the S4-S5 linker, which delimits the width of the pore domain. Once all four voltage sensors have transitioned into their "up" conformation, the pore is believed to open in a concerted, iris-like manner (Yifrach and MacKinnon, 2002; Labro et al., 2003). Voltage sensors of Kv channels have been found to be "portable" between Kv channels, suggesting that voltage sensitivity is independent from the gating of the pore domain (Alabi et al., 2007). Additionally, proteins homologous to the Kv voltage sensor have been found without a pore domain, giving further support to the notion that the voltage sensor and pore domain operate independently (Sasaki et al., 2006). Thus, the energetics of gating

the pore domain of Kv channels could reveal insights into the overall mechanism of gating in Kv channels. In this chapter, I will use targeted molecular dynamics (TMD) to generate a transition between the pore domains of the open crystal structure and a closed model of KvAP. Then, using intermediate configurations from the TMD simulations as initial conformations for umbrella sampling simulations, I will calculate the energetics of gating the KvAP pore domain.

4.2 Methods

The pore domain and S4-S5 linker of KvAP (PDB code 1ORQ), a 6-TM Kv channel, was used (residues 135 to 240) for the following simulations. The crystal structure, which exists in the open conformation, was used as the "open" conformation. The "closed" state was extracted from recent simulations modeling the closed state of KvAP (Schow et al., 2012).

Using the CHARMM-GUI web service, the protein was embedded in a POPC lipid bilayer (Jo et al., 2008). The system was solvated with the TIP3P water molecule and 150 mM KCl, totaling 60,781 atoms (Fig. 4.2). All simulations were carried out at a constant temperature of 303.15 K with Langevin dynamics and at 1 atm with the Langevin Nosé-Hoover method. The SHAKE algorithm was used to model high frequency hydrogen atom oscillations. All

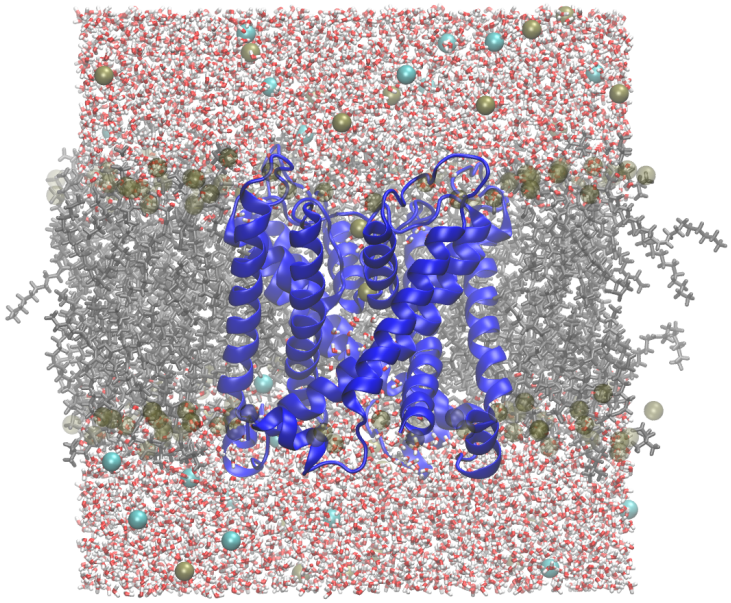

Figure 4.2: The simulation system used for TMD and umbrella sampling simulations. The KvAP crystal structure (PDB code 1ORQ) served as a template for the open protein structure. The protein consisted of residues 135 through 240.

simulations were run with the NAMD2.9 (Phillips et al., 2005)software package with the CHARMM36 force field (Best et al., 2012).

To delimit the width of the pore domain in the open and closed conformations, cross-pore harmonic restraints were applied to mimic LRET measurements of the S4-S5 linker in both the open and closed conformations of the KvAP channel (Faure et al., 2012). However, the sequence of the KvAP S4-S5 linker allowed for one fewer restraint in the open conformation than the simulations in Chapter 3. Additionally, the I414C mutant did not yield reliable

Table 4.1: Atomic distances for the S4-S5 linker in the closed conformations and open conformations of KvAP, as measured by LRET (and discussed in Chapter 3).

Atom ID	Closed KvAP	Open KvAP
F137C	33.4 ± 2.7	42.2 ± 0.3
L138C	42.8 ± 0.9	46.7 ± 0.6
S139C	40.2 ± 0.4	44.3 ± 0.1
I141C	N/A	41.9 ± 0.1
D143C	37.9 ± 1.5	42.4 ± 0.09
D146C	33.2 ± 1.1	41.9 ± 0.6

measurements in the closed conformation and, consequently, no restraints were applied to this residue in the closed simulations (Table 4.1).

Preliminary simulations (data not presented) suggested refinement of the closed structure was needed to maximize structural integrity of the protein. To that end, a four-fold symmetric tetramer was created by rotating each subunit about the membrane normal, creating an averaged monomer, and re-rotating each subunit about the membrane normal. Harmonic symmetry restraints were applied to the backbone of the resulting tetrameric structure. Additional restraints were applied to the carbonyls of the selectivity filter to maintain structural integrity during equilibration. To equilibrate the models, the systems were minimized, and backbone restraints were applied to the protein and gradually released. Each model (closed and open) was then simulated for 100 ns.

The resulting structures were used as end states for TMD simulations. TMD simulations were run from the open structure to the closed model, as well as from the closed model to

the open structure (thereby closing and opening the channel, respectively). TMD simulations were run for 200 ns each. Intermediate states from the TMD simulations were culled to be used as initial configurations for umbrella sampling simulations.

Umbrella sampling was used to generate statistics along the reaction coordinate to determine the energetic landscape of pore gating. The reaction coordinate for the gating transition was relative RMSD (rRMSD), defined as:

$$rRMSD = RMSD_{closed} - RMSD_{open}$$

$RMSD_{closed}$ represents the RMSD of the protein to the closed, equilibrated target structure, while $RMSD_{open}$ represents the RMSD of the protein to the open, equilibrated target structure. To promote greater conformational flexibility of the protein while tracking the gating process across the most physically relevant region of the protein, the residues included in the reaction coordinate were restricted to α carbons of the S4-S5 linkers, the interior of the S5 helix, and the interior of the S6 helix (residues 136-145, 150-167, 210-237, Fig. 4.3).

Windows were spaced 0.2 Å apart. Because each window was directly copied from a configuration in the TMD simulation, the systems have an identical composition to the TMD setup. Each window was simulated at 303.15 K with Langevin dynamics and at 1 atm with the Langevin Nosé-Hoover method. As in the TMD simulations, the SHAKE algorithm

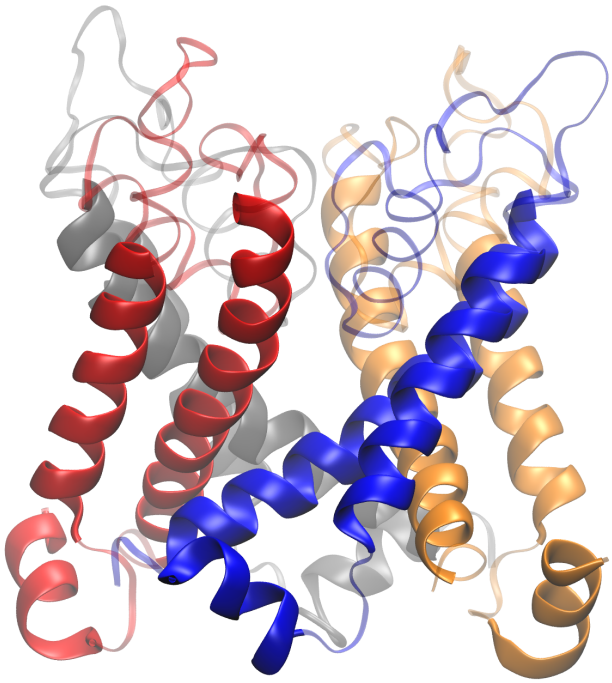

Figure 4.3: To localize the motions of KvAP relevant to the gating mechanism, the rRMSD reaction coordinate was calculated from the positions of the residues represented with a thick ribbon.

was used to represent hydrogen atom oscillations. All simulations were carried out with the NAMD2.9 software package with the CHARMM36 force field. Each window was simulated for 50 ns, with a harmonic restraint of 100 kcal/mol/Å^2. The free energy landscape was calculated using "WHAM: the weighted histogram analysis method", version 2.0.9 (Grossfield, 2014).

4.3 Results

Prior to the TMD simulations, well-equilibrated open and closed conformations were required to serve as target structures. In addition to the harmonic cross-pore restraints applied to the S4-S5 linker to induce open and closed S6 helices, harmonic symmetry restraints were applied to the backbone atoms to reduce minor local deformations of the protein structure. Additionally, cross-pore harmonic restraints applied to the carbonyls of the selectivity filter ensured that each selectivity filter maintained its activated conformation. After 100 ns of simulation of both the open and closed structures, the RMSD of each structure had plateaued (Fig. 4.4), suggesting a stable conformation suitable for beginning and end states of the subsequent TMD simulations (Fig. 4.5).

Most importantly, the S6 helix bundle crossings through which K^+ permeates were drastically different. The calculated radii of the pores of each structure reflect these drastically

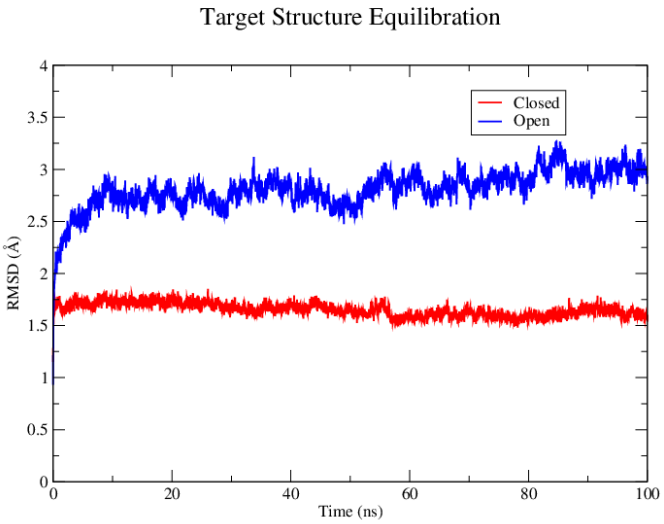

Figure 4.4: RMSDs of the open and closed target structures suggest well equilibrated structures after 100 ns simulations.

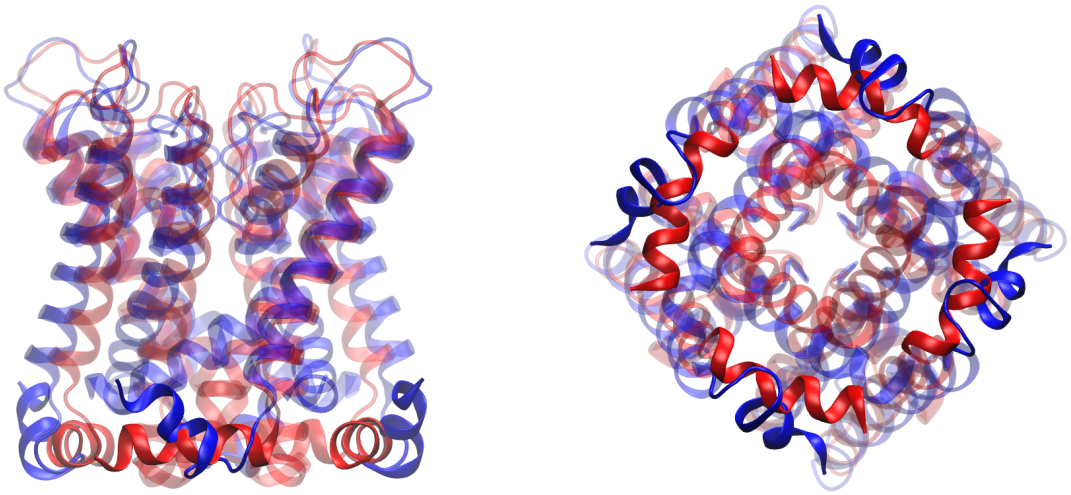

(a) (b)

Figure 4.5: The open (blue) and closed (red) target structures used for targeted molecular dynamics simulations. a) The S4-S5 linker adopts different orientations in the open and closed conformation. b) The ion permeation pathway is constricted by the S6 helix bundle crossing in the closed conformation.

different conformations; the radius of the pore in the open structure reduces until a constriction point along the selectivity filter, where K^+ is believed to be dehydrated before being coordinated through by the backbone carbonyls. In the closed structure, however, access to the selectivity filter is blocked by a sharp constriction point at residue 236Q, creating a barrier impermeable to a solvated K^+ (Fig. 4.6a). These calculated pore radii are used as a standard for subsequent definitions of "open" and "closed" pore conformations (Fig 4.6b).

The RMSD between the endpoints was 4.35 Å. Consequently, the rRMSD reaction coordinate must be sampled from -4.35 (closed) to 4.35 (open). In order to generate initial

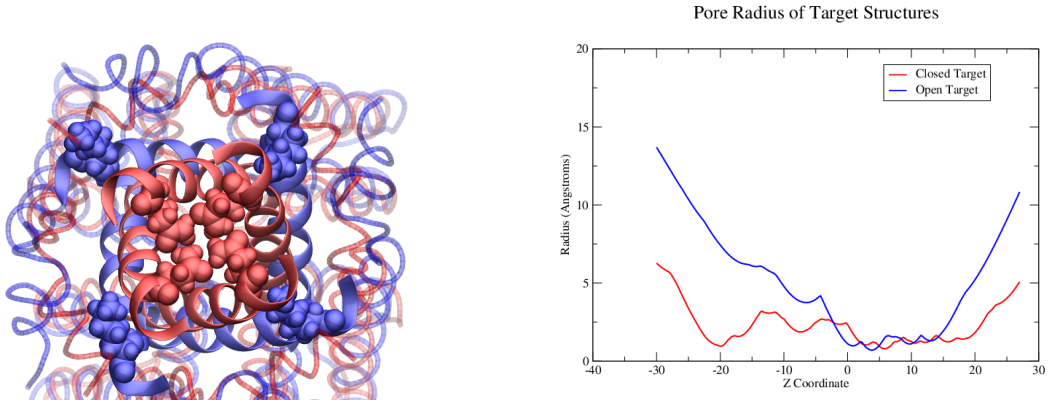

(a) (b)

Figure 4.6: The S6 gating helices create a constriction of the ion permeation pathway in the closed conformation. a) 236Q occludes the pore in the closed (red) conformation, hindering K^+ from passing through the channel. In the open conformation, 236Q is orientated away from the ion permeation pathway. b). In the open conformation, K^+ ions are funneled towards the selectivity filter. In the closed conformation, the restriction point around 236Q prevents solvated K^+ from permeating through the vestibule.

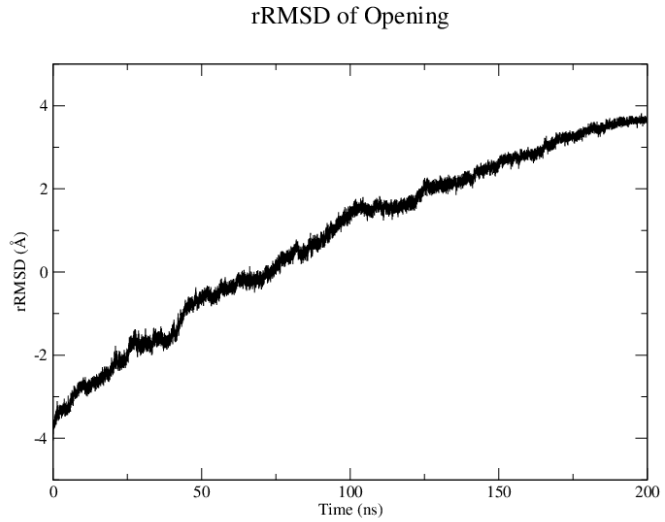

Figure 4.7: Targeted molecular dynamics simulations of the KvAP S4-S5 linker and pore domain sampled configurations across the entire rRMSD reaction coordinate to be used in umbrella sampling simulations.

configurations for umbrella sampling, it is essential that the TMD simulation spans the entire reaction coordinate. The calculated rRMSD for the 200 ns TMD simulation of the pore opening was indeed sufficient to sample across this reaction coordinate (Fig. 4.7).

The transition between the closed and open conformations of the pore domain required the movement of two regions of the protein: the S4-S5 linker, positioned along the lateral face of the intracellular region of the protein, and the S6 gating helix, forming the constriction point along the ion permeation pathway at the protein's interior. The S4-S5 linker was restrained by identical cross-pore distances to those discussed in Chapter 3. Consequently,

the 4 Å radial outward motion of the S4-S5 linker discussed in Chapter 3 was inherently imposed as a required motion in the transition pathway between the open and closed conformations of KvAP.

Unlike in the simulations from Chapter 3, the S4-S5 linker was untethered (and also unrestrained) at its N-terminus. Without a voltage sensor acting as payload, the S4-S5 linker was highly mobile. The S4-S5 linker adopted starkly different tilt angles in the open and closed conformations. In the open structure, the S4-S5 linker is tilted downward, creating a 135° angle from the membrane normal. The S4-S5 linker of the closed conformation, however, is nearly perpendicular to the membrane normal, sitting flush along the membrane-water interface (Fig. 4.5a). During the TMD simulation, the tilt angles of the S4-S5 linker of each subunit fluctuate, ultimately converging at the final 135° angle of the open conformation (Fig. 4.8).

To confirm that the reaction coordinate was accurately sampling a transition of the pore domain from conducting to non-conducting conformations, the pore radius was calculated for every fifth window along the reaction coordinate (Fig. 4.9). The radius of the pore increases as the reaction coordinate progresses from -4.0 to 4.0, indicating that the reaction coordinate selected is sufficient to capture a relevant transition between the closed and open states.

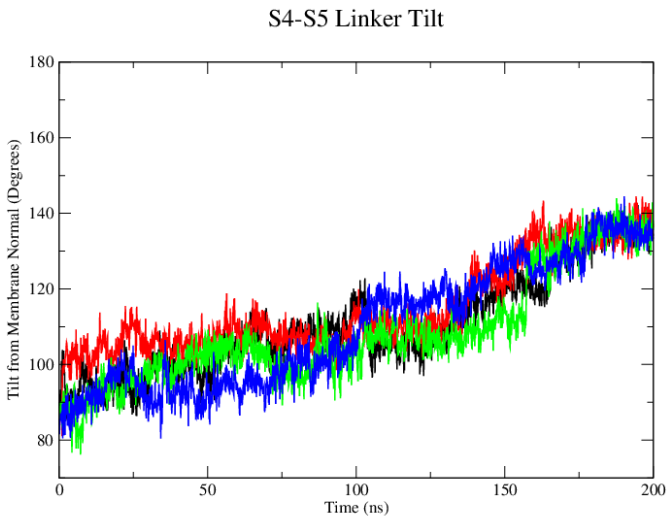

Figure 4.8: The S4-S5 linker tilts roughly 45° during the transition between the closed and open pore conformations. Beginning nearly perpendicular to the membrane normal, the S4-S5 linker pivots at its C-terminal end (near the S5 pore-lining helix), ultimately forming a roughly 135° angle to the Z-axis in the open conformation.

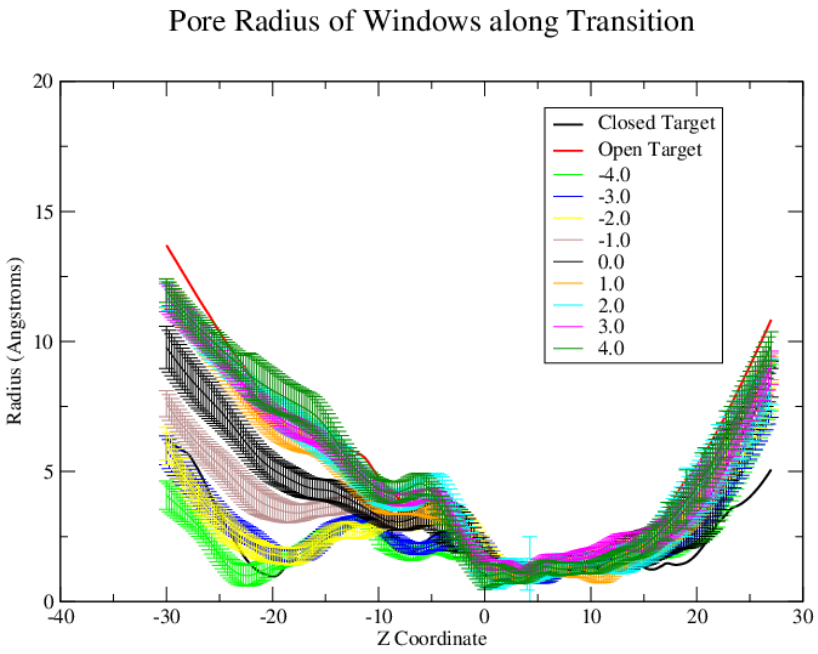

Figure 4.9: The rRMSD reaction coordinate is sufficient to describe the incremental opening of the KvAP pore domain. Here, the constriction of the pore domain decreases as the reaction coordinate increases from -4.0 (closed) to 4.0 (open).

The free energy profile of the opening of the KvAP pore domain was calculated using the weighted histogram analysis method (Grossfield, 2014). 40 ns/window was allowed for equilibration of the system; the final 10 ns were sampled to construct the free energy profile. Convergence of the free energy profile was verified by overlaying the free energy profiles of the final 10 ns, the final 5 ns, and the final 3 ns of the simulations. The histograms of each window indicate adequate sampling was obtained along the reaction coordinate (Fig. 4.10 a-c).

The free energy profile of the opening of the KvAP pore domain contains three minima: one around -3.0, one near 1.8, and one near -1.2 (Fig. 4.11). Pore radius calculations indicate that the minimum found near -3.0 reflects a closed, non-conducting conformation, while the minimum near 1.8 is an open, conducting conformation (Fig. 4.12). The minimum at -3.0 (“closed”), is approximately 2.7 kcal/mol higher in energy than the minimum at 1.8 (“open”). The minimum around rRMSD=-1.2 is an intermediate configuration with a partially opened pore (Fig. 4.12).

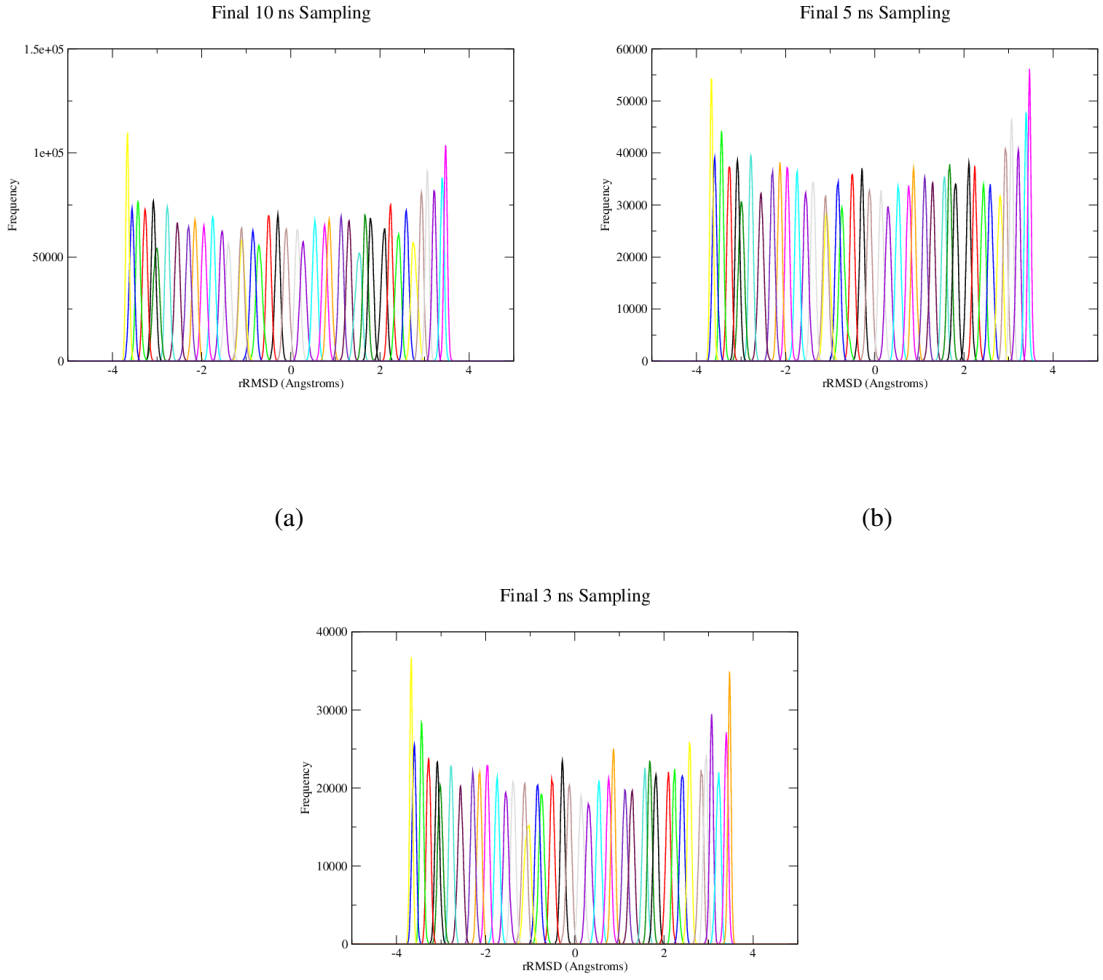

Figure 4.10: Histograms of the sampling for each window across the rRMSD reaction coordinate over the final a) 10 ns, b) 5 ns, and c) 3 ns of 50 ns umbrella sampling simulations.

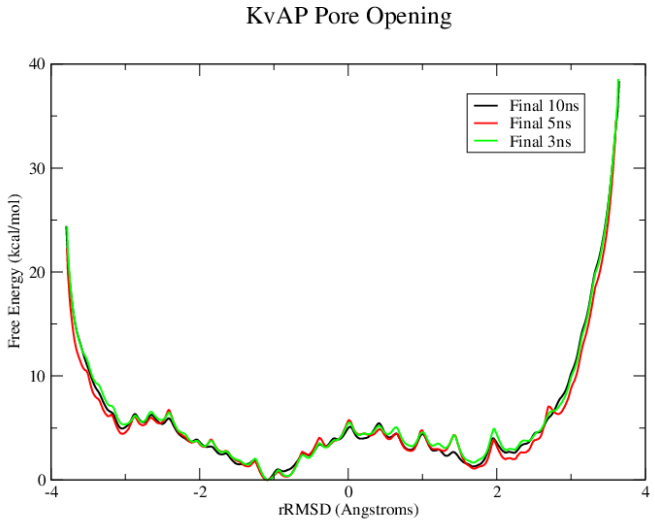

Figure 4.11: The free energy profile of KvAP pore domain opening.

4.4 Discussion

With the release of the first Kv channel x-ray crystal structures, hypotheses of the gating mechanism reached the atomic scale. The pore domain, which regulates both ion conduction and ion selectivity, is voltage insensitive. How, then, do the energetics of the pore domain contribute to the overall gating mechanism in Kv channels?

Though it is not without controversy, the general model of voltage sensitive gating in Kv channels states that, at the cellular resting potential, the voltage sensor is in its "down" conformation, depressed by the -70 mV transmembrane potential. As the cell depolarizes,

the voltage sensors undergo a transition into the "up" conformation. In this configuration, the S4-S5 linker is drawn outward, away from the S6 gating helices, inducing an opening of the channel as the S6 helices move away from one another. During repolarization, the voltage sensors are propelled back downward, pushing the S4-S5 linker downward and inward, sealing off the S6 helix bundle crossing and preventing ion permeation through the channel (Long et al., 2005a; Vargas et al., 2012).

Recent advances in supercomputing have finally allowed computational biophysicists to simulate the transition between an open Kv channel and its closed state. These simulations, however, suggested a different mechanism of deactivation: membrane depolarization drives the voltage sensor upward, forcing the linker outward and opening the pore. During deactivation, the pore domain undergoes a dewetting process, inducing a collapse of the S6 helices, closing the channel. The voltage sensors ultimately settle back in their down state (Jensen et al., 2012).

The energetic landscape presented here provides insight into the thermodynamics of the pore domain. The free energy profile shows three minima: closed, open, and an intermediate state. As with all umbrella sampling simulations, the energetic landscape is a function of the pathway taken along the reaction coordinate. Here, the targeted molecular dynamics simulation used to generate this pathway does not necessarily reflect the minimum free energy pathway between the closed and open conformations. TMD, a brute force method to

connect two endpoints, drives the system toward its endpoint with strong force constants and restraints that bias the system directly towards its predetermined endpoint, regardless of the energetics of the actual pathway. As a result, detailed energetic information of the physiological transition may be obfuscated.

The free energy profile presented here does contain features that reflect a canonical one-dimensional energy profile: an energetic minimum at the closed state, a second energetic minimum at the open state, and a small energetic barrier separating the two. Surprisingly, the global minimum along the free energy profile is at rRMSD=-1.2.

The configurations sampled at -1.2 reflect a partial opening of the pore domain. In this conformation, one subunit of the KvAP pore domain resembles the open conformation, while the other three subunits are closed (Fig. 4.12a). This partial outward motion of one subunit from the closed conformation partially opens the pore domain (Fig. 4.12b). For K^+ permeation to occur, the ions must be dehydrated before passing through the selectivity filter (Berneche and Roux, 2001). In the open conformation, ions are free to permeate through the cytosolic mouth of the channel and approach the selectivity filter unhindered. The selectivity filter, composed of backbone carbonyls, precisely coordinates the dehydrated K^+ ion through the filter, out of the channel, and into the extracellular solvent. The S6 helix bundle crossing cannot coordinate dehydrated K^+ ions, and, consequently, potassium ion permeation requires a pore radius wide enough to accommodate a solvated K^+. Though

the pathway sampled in the TMD simulations must be treated with skepticism, this minimum at -1.2 raises interesting questions: could the pore domain of Kv channels have an energetically favorable intermediate conformation?

The voltage sensors of Kv channels are well-documented to behave independently of one another (Gagnon and Bezanilla, 2009; Yeheskel et al., 2010). As the membrane depolarizes, the voltage sensors of Kv channels transition into their up state independently, ultimately transitioning into a "permissive" state in which all four voltage sensors have arrived at their up conformation. From this permissive state, the pore domain is free to open in a concerted, cooperative, iris-like motion (Zagotta et al., 1994; Schoppa and Sigworth, 1998; **?**). This pore opening converts the pore from a conformation in which all four S6 helices are closed into one in which all four are open. The energetic minimum at rRMSD=-1.2 is an interesting intermediate point. Recent free energy calculations considered the energetic barrier of ion permeation across the S6 helix bundle crossing as a function of pore radius. Intuitively, the energetic barrier to K^+ permeation decreased exponentially as pore radius increased (Fowler and Sansom, 2013). The rRMSD=-1.2 conformation could represent a non-conductive or minimally conductive intermediate in the gating process. Such a state suggests a pre-open configuration, in which one subunit of the pore domain has transitioned into its open state, presumably in response to the activation of the voltage sensor. By neutralizing the gating charges carried on three of the four S4 helices in Shaker (termed 1wt/3mut), it has been shown that voltage dependent gating does indeed still occur, though

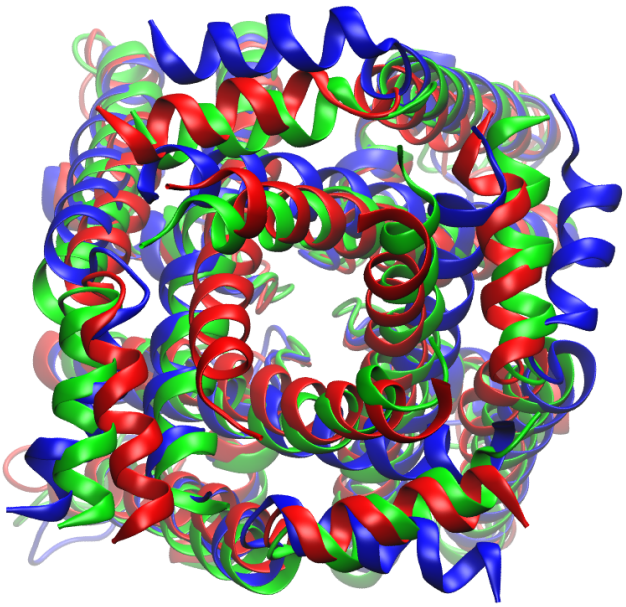

(a)

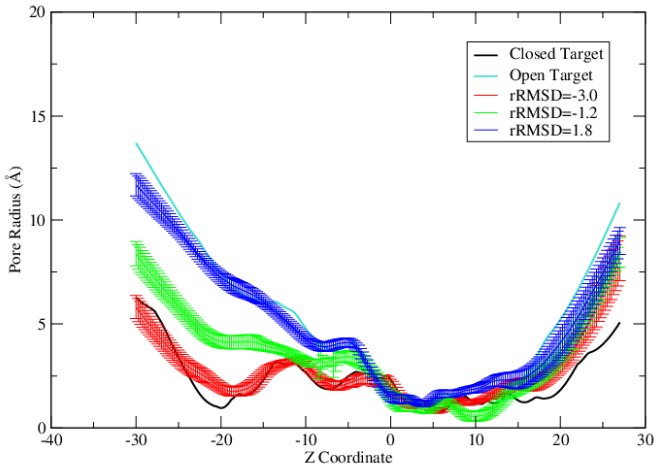

(b)

Figure 4.12: The free energy profile of the gating of the KvAP pore domain contains three minima: rRMSD=-3.0, a closed conformation (red); rRMSD=1.8, an open conformation (blue), and rRMSD=-1.2, an intermediate conformation (green). a). The rRMSD=-1.2 intermediate assumes a closed conformation in three subunits, while the fourth (rightmost in the figure) resembles the open configuration. b). The pore radii of the three minima reflect the closed, open, and intermediate pore conformations.

K^+ conductance is below the maximum K^+ conductance for a fully open channel (Gagnon and Bezanilla, 2009). Similar experiments neutralizing the gating charges on one subunit (3wt/1mut) could facilitate the formation of a similar pre-open state. As ion conduction is determined by the pore radius, such a pre-open state could expedite ion permeation in Kv channels. One dimensional free energy calculations of ion permeation could provide insights into the conductivity of this rRMSD=-1.2 conformation, and could be compared to the K^+ conductance of the 3wt/1mut channel to better understand this energetic minimum.

The sampling near the endpoints can provide insights into the relative free energies between the open and closed pore domains. The free energy profile generated from the umbrella sampling simulations presented here indicate that the closed pore domain is roughly 2.7 kcal/mol higher in free energy than the open conformation. How, then, could the energetic landscape of the pore domain contribute to the overall gating mechanism in Kv channels?

The S4-S5 linkers provide insight into the overall gating mechanism in KvAP. Studies of Kv channel voltage sensors have suggested S4 motions between 2 Å and 20 Å (Larsson et al., 1996; Ruta et al., 2005; Ahern and Horn, 2005; Vargas et al., 2011). With only lateral, cross-pore restraints applied to the S4-S5 linker, the N-terminus was free to orient itself in its most favorable orientation along the Z-axis. As the channel opened, the S4-S5 linker spontaneously tilted. The N-terminal end of the linker, to which the S4 voltage sensing helix is attached, moved roughly 3 Å upward as the pore domain opened (Fig. 4.13),

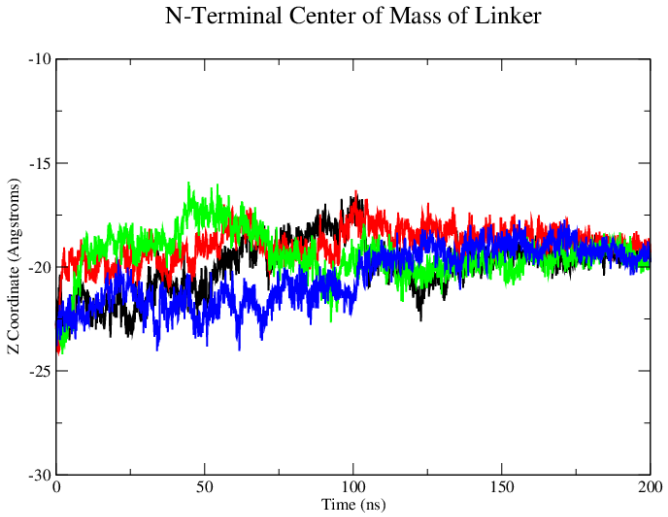

Figure 4.13: The S4-S5 linker undergoes a modest vertical displacement during the transition between the closed and open states.

in agreement with the more conservative estimations of voltage sensor motion during Kv channel activation (Chanda et al., 2005).

Experimental studies of the Kv pore domain have focused largely on the Shaker channel. Studies of Shaker's temperature dependence revealed that the open conformation is 1.6 kcal/mol lower in free energy than the closed conformation (Rodriguez et al., 1998), in strong agreement with the free energy profile presented here. However, the Shaker channel contains a PVP motif, a primary structural element which forms a hinge-like secondary structure on the S6 helices. Alanine mutagenesis studies of Shaker revealed that the closed conformation is energetically favorable to the open conformation (Yifrach and MacKinnon,

2002). Further study, however, found that the proline residues in the PVP motif are essential for this thermodynamic equilibrium; glycine and alanine mutants of the prolines within the PVP motif caused a rightward shift of the Shaker GV curve, indicating that this PVP motif is necessary for gating in Shaker channels. Furthermore, shifts of the PVP motif in the S6 sequence were sufficient to regain wildtype-like activation (Labro et al., 2003). KvAP does not have such a PVP motif, and, as a result, the underlying mechanism of pore domain gating may differ.

Similar free energy calculations were recently reported for the Kv1.2/2.1 chimera (Fowler and Sansom, 2013). In this study, the Kv1.2/2.1 chimera pore domain (without the S4-S5 linkers) was equilibrated and the free energy of gating was calculated by closing the channel. The authors found a nearly exponential increase in free energy as the channel was closed, leading them to conclude that the pore domain is forced closed by the voltage sensors and the S4-S5 linkers surrounding the pore applying an inward pressure against the S6 helices. The proteins studied may account for differences in the free energy landscapes. The Kv1.2/2.1 chimera contains a PVP motif in the S6 helices, which may alter gating energetics and produce a different free energy profile than KvAP.

The transition between the open and closed conformations could also contribute to the conflicting free energy profiles. Fowler and Sansom studied the closing of the pore domain, while the results presented here reflect the opening of the pore domain. Though

the fundamental motions of opening and closing the KvAP pore domain are identical (inward/outward motion of S4-S5 linker, inward/outward motion of S6 helices), the solvent effects on the system could influence the free energy landscape. In Fowler and Sansom's work, only 10 ns was used to equilibrate the system, and statistics for each window were collected for 1 ns. This experimental protocol could result in a trapping of water within the pore domain, straining the S6 helices and influencing them to move outward (shifting the energetic landscape to favor the open conformation).

To evaluate the effects of the pathway on the number of water molecules within the pore domain, a 200 ns TMD simulation was used to close the channel from its open conformation. In order to exclude water from the pore domain when closing the channel, ample equilibration is needed. Even with 200 ns simulations, the number of pore water molecules during the opening and closing process do not mirror one another (Fig. 4.14). Shorter simulations, such as those by Fowler and Sansom, could be influenced by strong solvent effects. Jensen et al., reaching simulation times in the hundreds of microseconds, proposed that a dewetting process of the pore domain is essential for S6 helix closure (Jensen et al., 2012). The exponentially increasing energetic landscape of Fowler and Sansom could reflect this necessary process. The pore domain has a limited volume, and certainly contains a maximum solvent capacity. It will be essential to determine the most energetically favorable pore hydration states along the transition pathway to accurately quantify the gating energetics and the fundamental mechanism of Kv channels.

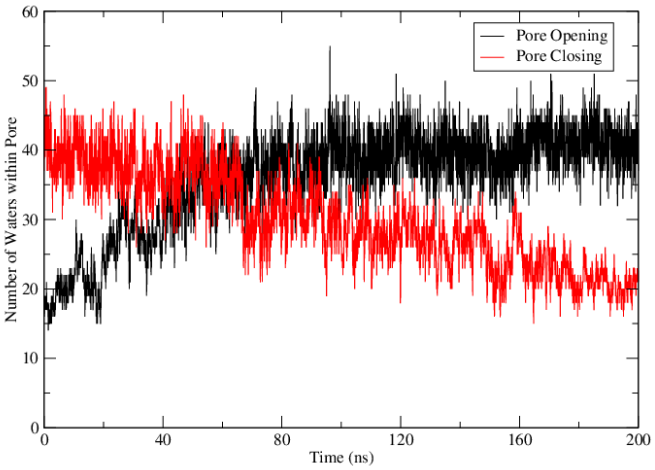

Figure 4.14: The number of water molecules within the KvAP pore domain is dependent upon the gating pathway, and could ultimately influence the free energy landscape.

Chapter 5

Membrane Binding of VSTx1, a Voltage Sensor Toxin

5.1 Introduction

In the evolutionary arms race between predator and prey, a variety of attack and defense mechanisms have evolved to increase the fitness of both the hunter and the hunted. While the brute force of speed and strength are among the more visceral examples of this battle for survival, evolution also occurs on the molecular level to increase the lethality–and

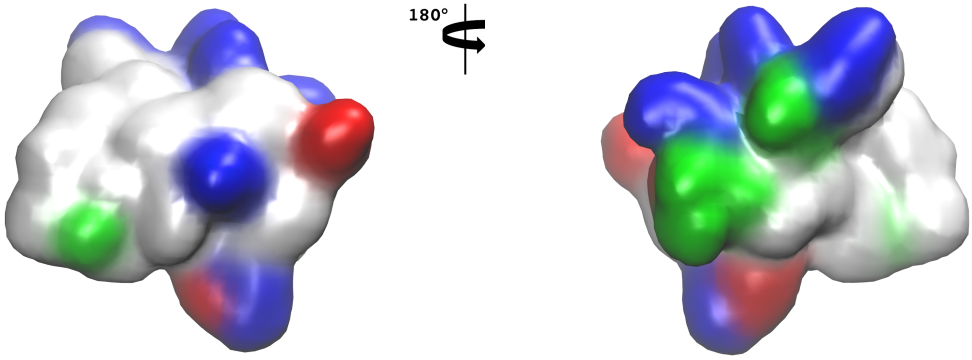

Figure 5.1: VSTx1, a tarantula toxin and member of the ICK family of proteins.

fitness–of both predator and prey, large and small. Toxins–endogenously produced chemical compounds that produce an adverse effect in other organisms–are used by both predator and prey alike. In the plant kingdom, where mobility is limited, toxins are especially useful for defense. Banana trees localize phenylphenalenones in their roots to poison parasitic nematodes in the soil (Hölscher et al., 2014). In the animal kingdom, skunks release noxious chemical toxins to ward off potential attackers (Wood, 1990). To stun, paralyze, and even kill, certain species of tarantula inject neurotoxins into their prey.

Tarantula venom contains toxins that affect a variety of membrane channels: voltage-gated cation channels (Lampe et al., 1993), ligand-gated ion channels (Baconguis and Gouaux, 2012), and mechanosensitive stretch-activated ion channels (Bae et al., 2011). Containing multiple disulfide bonds bridging the protein, these short peptides of 30-40 amino acids are classified as members of the inhibitor cysteine knot (ICK) family.

VSTx1, an ICK protein found in tarantula venom, significantly alters the gating kinetics of voltage gated potassium ion channels, namely KvAP. In the presence of VSTx1, the activation of KvAP is significantly hindered, resulting in a right-shifted G-V curve. Consequently, tarantula toxins, and VSTx1 in particular, are useful probes of voltage gated ion channel properties. VSTx1, for example, has been useful in both structural and functional studies of Kv channels (Alabi et al., 2007).

Though the mode of action is unclear, many tarantula toxins are believed to partition into the lipid membrane in order to act on their target. For example, GsMTx4, an ICK tarantula toxin inhibiting stretch activated cation channels, inhibits stretch activated channels (SAC) in both its D and L enantiomers. Because the affinity of the toxin to the protein shows no apparent chiral preference, GsMTx4 most likely partitions into the neighboring lipid membrane, altering the lateral surface tension of the lipid membrane on the SAC protein, thereby inhibiting its native function (Posokhov et al., 2007). Similarly, VSTx1 is believed to alter the interactions and lateral forces between the membrane and the voltage sensor (Schmidt and MacKinnon, 2008).

To determine the atomic level interactions between a tarantula toxin and a lipid membrane, I perform molecular dynamics simulations recreating the experimental setup of neutron

scattering experiments. Using the neutron scattering density profile of VSTx1 in a multilayer as a restraint for MD simulations of VSTx1, I present an atomistic model of VSTx1 binding with the lipid bilayer.

5.2 Methods

All simulations were carried out to replicate the experimental conditions of the neutron scattering study. One VSTx1 peptide (PDB code 1S6X) was placed on each side of the lipid bilayer (two toxins in total). 112 POPC lipids were used to create the membrane bilayer. A total of 1043 TIP3 water molecules were seeded just beyond the lipid headgroups. Periodic boundary conditions were applied in all directions.

The simulations were run using the NAMD 2.9 software package (Phillips et al., 2005) with the CHARMM36 force field. Temperature was held constant at 295 K with Langevin dynamics. Pressure was maintained at 1 atm with Langevin Nosé-Hoover method. The SHAKE algorithm was used to model the high frequency oscillations of hydrogen atoms. The simulations were run for 120 ns; analysis was conducted on the final 37 ns of simulation, as they represent the fully equilibrated system.

Restraints were applied to the protein according to the experimentally determined transbilayer distribution, $\rho(Z)$. To accurately recapitulate the experimentally determined densities, a dynamic force was applied to selectively deuterated hydrogen atoms from the experiment (8 H atoms on F5, 3 H atoms on M6, 5 H atoms on F7, 8 H atoms on V29, and 10 H atoms on L30, collectively referred to as "patch"). To determine the forces applied to each atom, a pseudo-potential, $\Phi(Z) = 1 - \rho(Z)$, was generated. Finally, a force profile along the Z-axis, F(Z), was created by taking the negative derivative of the pseudo-potential, $F(Z) = -\frac{d\Phi}{dZ}$. At each step in the simulation, the Z coordinate of the deuterated patch residues was checked against F(Z) and a specific force was applied to each deuterated atom.

5.3 Results

The scattering density profile for the simulation closely matches the experimentally-determined scattering density profile (Fig. 5.2). Strong qualitative agreement exists between simulation and experiment for the distributions of the deuterated residues of the toxin's hydrophobic patch, the water molecules, the D4 residues on the POPC lipids, and the sum total of all of the system's components. Though slight deviations can be seen between the experimental and computational scattering density profiles of the D4 atoms near

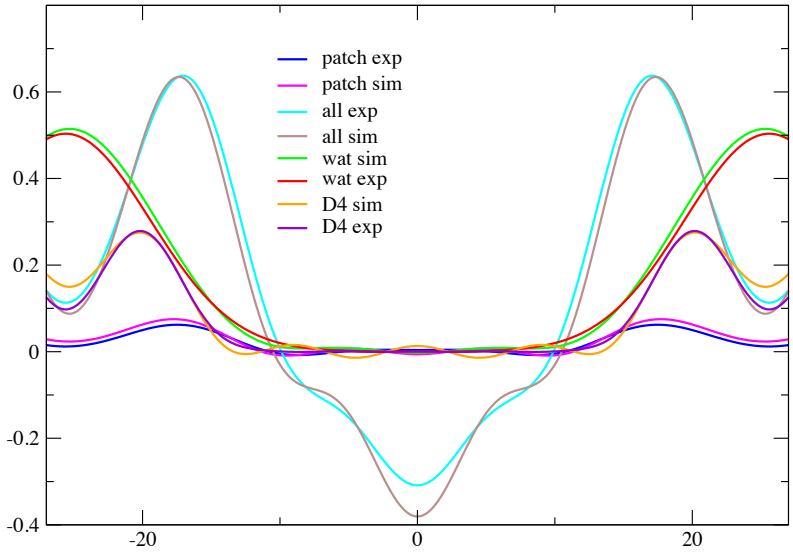

Figure 5.2: The calculated scattering density profile from simulation is in good agreement with the experimentally determined profile.

the boundaries of the system, this discrepancy may well be due to different lipid composition (100% POPC in simulation, 50:50 POPC:POPG mixture in experiment).

Density profiles calculated from the simulation reveal unique phases on each side of the membrane leaflet. The phosphate and carbonyl peaks of the POPC lipids of the upper leaflet are broader than those of the lower leaflet, indicating a larger membrane deformation of the upper leaflet. Additionally, the distribution of water around the upper leaflet is also wider, fully hydrating the lipid phosphates (Fig. 5.3). The distribution of water within the bilayer is also different along the upper and lower leaflets of the membrane. Though the

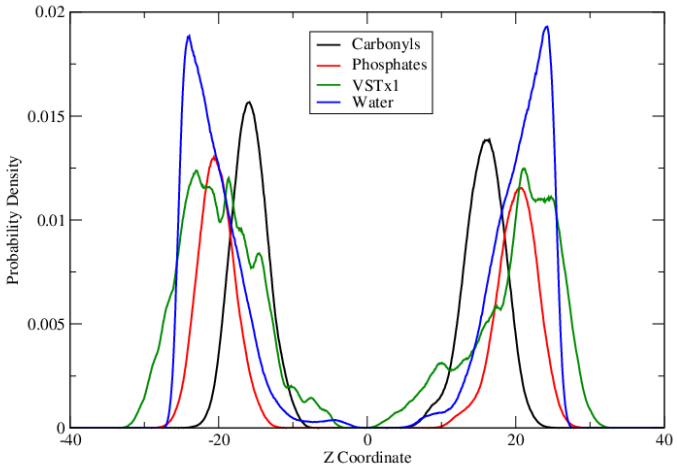

Figure 5.3: Density profile of VSTx1 simulations. Asymmetry in component distributions suggests alternative binding modes of VSTx1 to the membrane interface.

water density peak of the lower leaflet is narrower than that of the upper leaflet, it features a shoulder which extends well into the center of the bilayer, peaking slightly around Z=-3.

Two dimensional histograms reveal the deformation of the upper leaflet (Fig. 5.4). While the topology of the lower leaflet is mostly homogenous, the upper leaflet shows a deep well near the protein (whose center of mass is centered at 0, 0, Z).

The different topologies of the lower and upper leaflets induce differing orientations of the toxins of the lower at each membrane interface. The cavity created along the upper leaflet allows for a more modest insertion of VSTx than the more planar lower leaflet. VST1, the

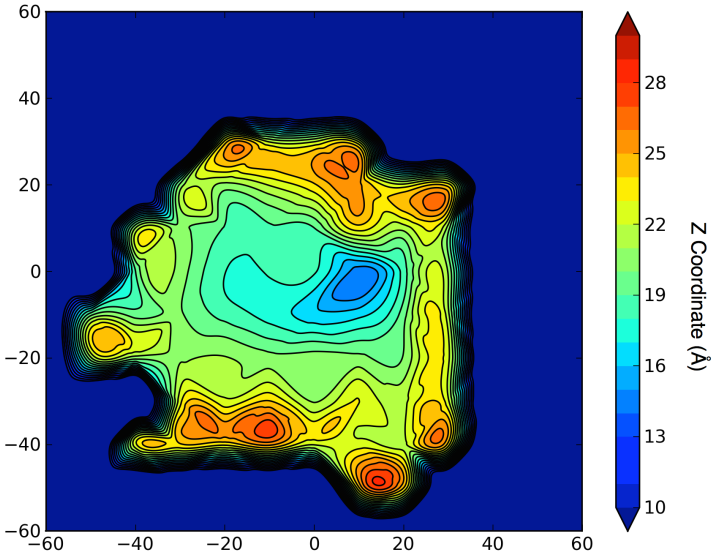

(a)

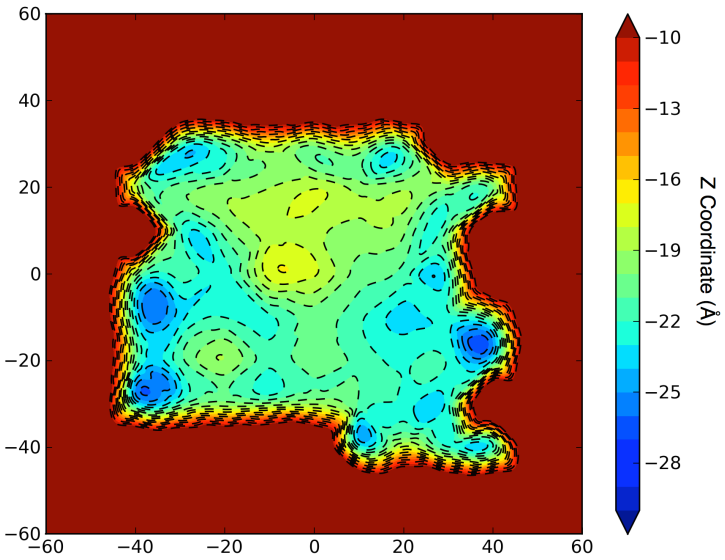

(b)

Figure 5.4: The upper leaflet of the lipid bilayer (a) forms a cavity around and beneath the VSTx toxin peptide, while the lower leaflet (b) maintains a more planar conformation.

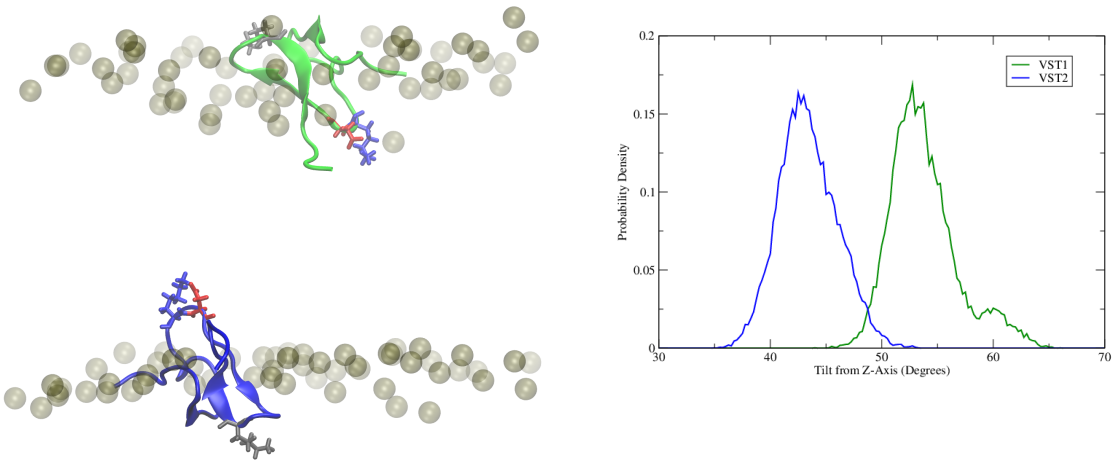

(a) (b)

Figure 5.5: VST1 and VST2, toxins on the upper and lower leaflets, respectively, assume different orientations relative to the membrane normal. a). VST1, green, is more flush with the membrane normal. b). Using the axis formed between residues K17 and R24 as a reference, VST1 (green) tilts approximately 15° further from the membrane normal than VST2 (blue).

toxin positioned along the upper leaflet, is more flush with the membrane than VST2 (the toxin positioned along the lower leaflet) (Fig. 5.5).

Though the toxins assume different orientations, they do not undergo any significant conformational changes. RMSDs of the toxins in the simulations show only small fluctuations in peptide backbone structure (Fig. 5.6a). Additionally, salt bridge analysis reveals no major rearrangements of the protein sidechains (Fig. 5.6b). In both VST1 and VST2, the salt bridge between K17 and D18 endures throughout the entire simulation.

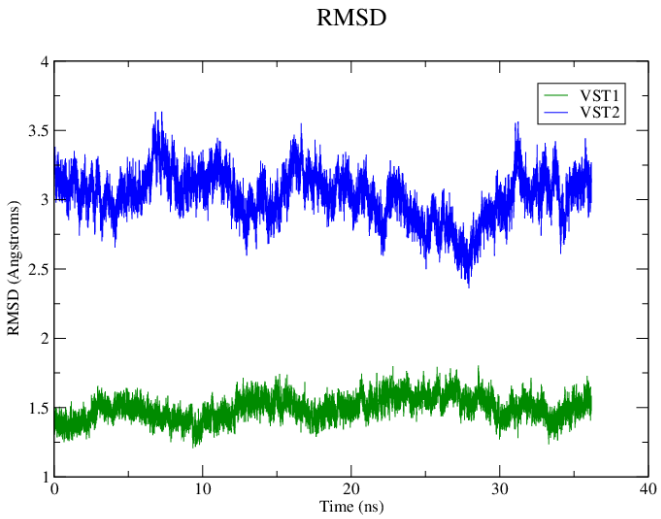

(a)

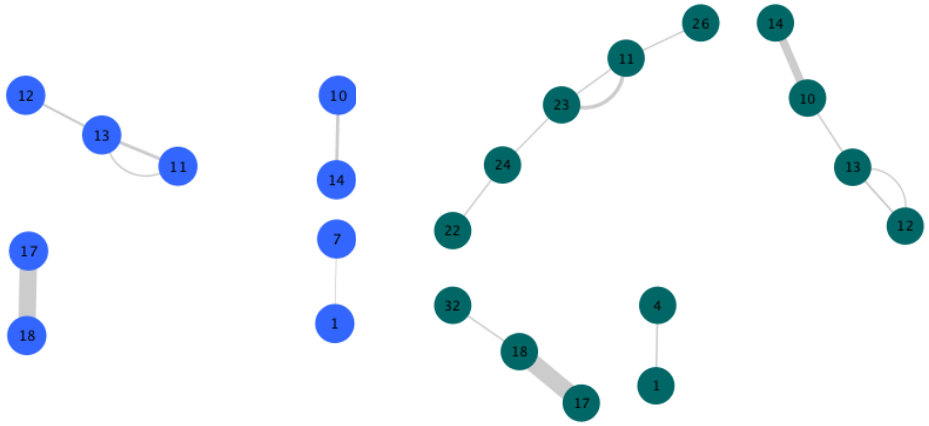

(b)

Figure 5.6: The VSTx peptides are stable during the final 40 ns of simulation. a). The RMSDs for each peptide in the simulation (VST1 and VST2) are stable, indicating no large conformational changes. b). The K17-D18 salt bridge is robust in both VST1 (green) and VST2 (blue).

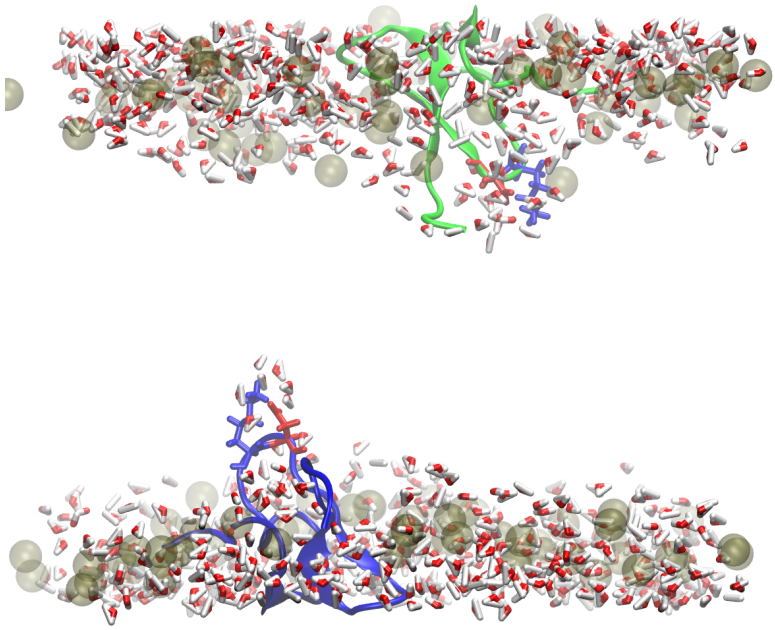

Figure 5.7: The differing orientations of VST1 and VST2 affect the depth of the K17 (blue) - D18 (red) salt bridge pair.

The K17-D18 salt bridge is thoroughly solvated throughout the simulation (Fig. 5.7). Along the upper leaflet, where the toxin lies more flush with the plane of the membrane, K17 and D18 are positioned closer to the headgroup region of the bilayer. In this orientation, in addition to hydration from the water molecules occupying the cavity created by the membrane deformation, a phosphate from the lipid headgroups interacts with K17. On the lower leaflet, the more vertical orientation of VST2 forces K17 and D18 deeper into the membrane. Too deep within the hydrocarbon core of the membrane to interact with headgroups, the K17-D18 salt bridge of VST2 is solvated only by water molecules.

5.4 Discussion

Given their role in regulating neuronal activity, voltage sensors of voltage gated ion channels are ideal neurotoxic targets for predators (Swartz and MacKinnon, 1995; Cestèle et al., 1998; Li-Smerin and Swartz, 2000; Jung et al., 2005). Because VSTx1, a tarantula toxin, significantly alters the gating of KvAP, a prokaryotic Kv channel (Ruta and MacKinnon, 2004), the structural interactions of the toxin with the voltage sensor of KvAP may be universal to all Kv channel voltage sensors. Mutagenesis studies of the voltage sensor domain revealed that the S3b and S4 helices are involved in the mode of action of VSTx1 on Kv channels (Alabi et al., 2007). VSTx1 is believed to interact with the voltage sensor after first partitioning into the membrane (Milescu et al., 2007). At present, the mode of interaction of VSTx1 with the lipid membrane is unclear.

The orientation of the toxin seen in the simulations could facilitate its mode of action on the Kv voltage sensor. The most surprising result was the burial of the hydrophilic residues K17 and D18. However, these two polar residues engage in a salt bridge throughout the simulation, and are further solvated by water and lipid phosphate. VSTx1 contains five basic residues, and the orientation seen in the simulations positions the remaining four basic residues in the aqueous extracellular solvent (Fig. 5.8).

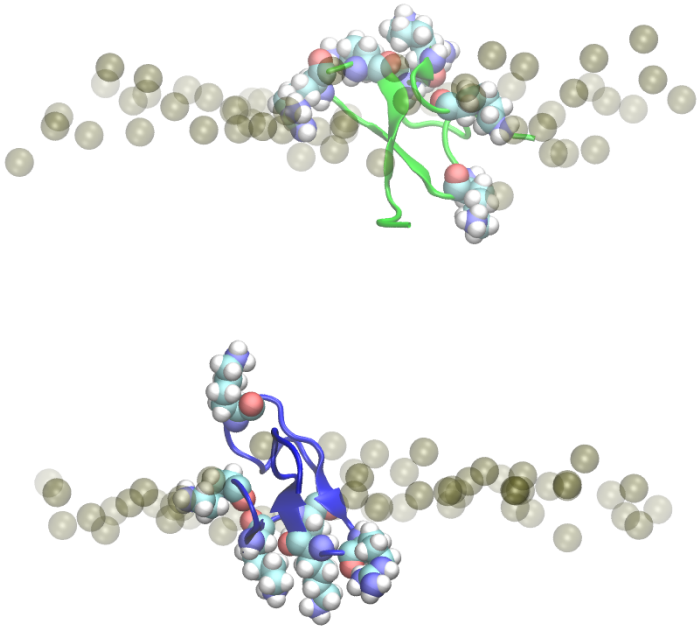

Figure 5.8: Though the K17-D18 salt bridge is buried within the hydrocarbon core of the membrane, the orientation of the toxin seen in the simulation positions the toxin's four remaining basic residues in the extracellular aqueous solvent.

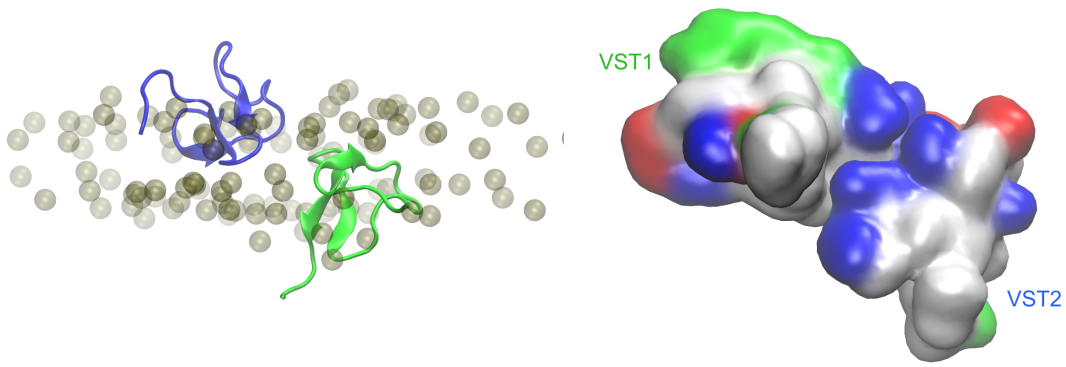

(a) (b)

Figure 5.9: Though separated by the membrane bilayer, VST1 (along the upper leaflet) comes in contact with the periodic image of VST2 of the neighboring unit cell.

Though the molecular dynamics simulations recreate the experimentally-observed scattering density profile, the setup of the simulations could ultimately influence the computationally-derived scattering density profile. Though they exist on opposite membrane leaflets, the periodic nature along the Z axis of the minimally-hydrated multilayer positions VST1 within close proximity of VST2 of the adjacent unit cell. An unfavorable interface exists between VST1 and VST2, and electrostatic mismatch along the toxin interface could drive the membrane deformation of the upper leaflet (Fig. 5.9).

Mutagenesis studies of SGTx1, an ICK tarantula toxin which also targets Kv channels (Lee et al., 2004), revealed a cluster of residues which drastically affect Kv channel gating (Wang et al., 2004; Milescu et al., 2007). Intriguingly, when superposed onto VSTx1 in its

simulated orientation, these residues are clustered together along the same lateral face of the toxin. This orientation could facilitate a lateral interaction between a membrane bound toxin and the Kv voltage sensor.

Chapter 6

Concluding Remarks

The x-ray crystalization of Kv channel crystals over the past decade revealed structural information of 6TM K^+ channels at atomic resolution. The atomistic information of these structures also provided new insights into functional mechanisms of the channels. Nevertheless, these crystal structures are static configurations–mere snapshots arranged in a highly ordered lattice. To approach the functional mechanisms of Kv channels, dynamic information is essential.

In Chapter 2, I simulated a Kv voltage sensor with its S4 helix in 3_{10} and alpha conformations to assess the plausibility that an interconversion between the alpha and 3_{10} conformations could account for experimental measurements of voltage sensor motions during

channel gating. This 3_{10} to alpha conversion would cause the S4 helix to elongate, rotate, and tilt, in agreement with experimental evidence.

In Chapter 3, I applied the 3_{10} and alpha restraints to a full Kv channel and found that, on the timescales attainable, this secondary structure interconversion does not alter the state of the pore domain. I also used the full Kv1.2/2.1 chimera channel to model luminescence resonance energy transfer measurements of the S4-S5 linker in the closed state. These positional restraints were sufficient to induce conformational changes of both the S6 helices by closing the channel, and also the voltage sensor. The resulting structure recapitulated a number of experimentally determined measurements of the closed Kv channel conformation.

In Chapter 4, I used the same experimentally determined values of the S4-S5 linker from Chapter 3 to model the KvAP pore domain in its closed state. I then used targeted molecular dynamics to generate a transition between the closed and open conformations of the pore domain. This transition allowed me to perform umbrella sampling simulations of the gating transition in KvAP, and I found that the open conformation is energetically favorable to the closed pore (2.7 kcal/mol).

In Chapter 5, I use experimentally-determined one-dimensional neutron scattering data of the VSTx1 toxin to generate restraints for molecular dynamics simulations. Because the scattering density profiles of simulation closely matches the experimental scattering

density profile, I can extract three dimensional structural information from the molecular dynamics simulations. These simulations provide insight into the binding of VSTx1 to the lipid bilayer.

From a set of initial coordinates, molecular dynamics simuations are able to predict the positions and momenta of hundreds of thousands of atoms, limited only by the empirically-determined parameters used in the simulation and the computational power available to the scientist performing the experiment. Consequently, molecular dynamics is often described as an atomic microscope–a tool capable of resolving fully atomistic infomation over a given period of time.

Though molecular dynamics does indeed project the behavior of hundreds of thousands of atoms, its true versatility is in its ability to create, quantify, and explore the unknown. In each chapter in this dissertation, molecular dynamics is used as starting point to generate as-of-yet unknown three dimensional structures. Then, simply by applying Newton's laws of motion, molecular dynamics can predict behaviors of theoretical structures (Chapters 2, 3, and 4), quantify energetics (Chapter 4), and turn one-dimensional information into three dimensional, time-resolved data (Chapters 3 and 5). Molecular dynamics is much more than just a microscope capable of peeking into the molecular world; it allows us to create a molecular world, preceisely monitor all of its components, witness its behaviors

on a human timescale, and extract information otherwise undetectable by experimental techniques.

Bibliography

Ahern, C. A. and Horn, R. (2005). Focused electric field across the voltage sensor of potassium channels. Neuron *48*, 25–9.

Alabi, A. A., Bahamonde, M. I., Jung, H. J., Kim, J. I. and Swartz, K. J. (2007). Portability of paddle motif function and pharmacology in voltage sensors. Nature *450*, 370–375.

Baconguis, I. and Gouaux, E. (2012). Structural plasticity and dynamic selectivity of acid-sensing ion channel-spider toxin complexes. Nature *489*, 400–405.

Bae, C., Sachs, F. and Gottlieb, P. A. (2011). The mechanosensitive ion channel Piezo1 is inhibited by the peptide GsMTx4. Biochemistry *50*, 6295–6300.

Berman, H. M., Westbrook, J., Feng, Z., Gilliland, G., Bhat, T., Weissig, H., Shindyalov, I. N. and Bourne, P. E. (2013). PDB Current Holdings Breakdown. http://www.rcsb.org/pdb/statistics/holdings.do (accessed January 2, 2014).

Berneche, S. and Roux, B. (2001). Energetics of ion conduction through the K+ channel. Nature *414*, 73–77.

Best, R. B., Zhu, X., Shim, J., Lopes, P. E. M., Mittal, J., Feig, M. and MacKerell, A. D. (2012). Optimization of the Additive CHARMM All-Atom Protein Force Field Targeting Improved Sampling of the Backbone , ψ and Side-Chain $\chi 1$ and $\chi 2$ Dihedral Angles. J Chem Theory Comput *8*, 3257–3273.

Bezanilla, F. (2000). The voltage sensor in voltage-dependent ion channels. Physiol Rev *80*, 555–92.

Blunck, R. and Batulan, Z. (2012). Mechanism of electromechanical coupling in voltage-gated potassium channels. Front Pharmacol *3*, 166.

Brooks, B. R., Brooks, C. L., Mackerell, A. D., Nilsson, L., Petrella, R. J., Roux, B., Won, Y., Archontis, G., Bartels, C. and Boresch, S. (2009). CHARMM: the biomolecular simulation program. Journal of computational chemistry *30*, 1545–1614.

Caffrey, M. (2003). Membrane protein crystallization. Journal of Structural Biology *142*, 108–132.

Campos, F. V., Chanda, B., Roux, B. and Bezanilla, F. (2007). Two atomic constraints unambiguously position the S4 segment relative to S1 and S2 segments in the closed state of Shaker K channel. Proceedings of the National Academy of Sciences *104*, 7904–7909.

Carpenter, E. P., Beis, K., Cameron, A. D. and Iwata, S. (2008). Overcoming the challenges of membrane protein crystallography. Curr Opin Struct Biol *18*, 581–6.

Cestèle, S., Qu, Y., Rogers, J. C., Rochat, H., Scheuer, T. and Catterall, W. A. (1998). Voltage sensor-trapping: enhanced activation of sodium channels by beta-scorpion toxin bound to the S3-S4 loop in domain II. Neuron *21*, 919–31.

Chanda, B., Asamoah, O. K., Blunck, R., Roux, B. and Bezanilla, F. (2005). Gating charge displacement in voltage-gated ion channels involves limited transmembrane movement. Nature *436*, 852–856.

Clayton, G. M., Altieri, S., Heginbotham, L., Unger, V. M. and Morais-Cabral, J. a. H. (2008). Structure of the transmembrane regions of a bacterial cyclic nucleotide-regulated channel. Proceedings of the National Academy of Sciences *105*, 1511–1515.

Cohen, B. E., Grabe, M. and Jan, L. Y. (2003). Answers and questions from the KvAP structures. Neuron *39*, 395–400.

Delemotte, L., Tarek, M., Klein, M. L., Amaral, C. and Treptow, W. (2011). Intermediate states of the Kv1. 2 voltage sensor from atomistic molecular dynamics simulations. Proceedings of the National Academy of Sciences *108*, 6109–6114.

Enkhbayar, P., Hikichi, K., Osaki, M., Kretsinger, R. H. and Matsushima, N. (2006). 310-helices in proteins are parahelices. Proteins: Structure, Function, and Bioinformatics *64*, 691–699.

Faure, E., Starek, G., McGuire, H., Berneche, S. and Blunck, R. (2012). A limited 4 Åradial displacement of the S4-S5 linker is sufficient for internal gate closing in Kv channels. Journal of Biological Chemistry *287*, 40091–40098.

Fowler, P. W. and Sansom, M. S. P. (2013). The pore of voltage-gated potassium ion channels is strained when closed. Nat Commun *4*, 1872.

Gagnon, D. G. and Bezanilla, F. (2009). A single charged voltage sensor is capable of gating the Shaker K+ channel. J Gen Physiol *133*, 467–83.

Grossfield, A. (2014). WHAM: the weighted histogram analysis method, Version 2.0.9.

Hackos, D. H., Chang, T.-H. . H. and Swartz, K. J. (2002). Scanning the intracellular S6 activation gate in the shaker K+ channel. The Journal of general physiology *119*, 521–531.

Haddad, G. A. and Blunck, R. (2011). Mode shift of the voltage sensors in Shaker K+ channels is caused by energetic coupling to the pore domain. The Journal of general physiology *137*, 455–472.

Henrion, U., Renhorn, J., Börjesson, S. I., Nelson, E. M., Schwaiger, C. S., Bjelkmar, P., Wallner, B., Lindahl, E. and Elinder, F. (2012). Tracking a complete voltage-sensor cycle with metal-ion bridges. Proceedings of the National Academy of Sciences *109*, 8552–8557.

Hodgkin, A. L. and Huxley, A. F. (1952). A quantitative description of membrane current and its application to conduction and excitation in nerve. J Physiol *117*, 500–44.

Hölscher, D., Dhakshinamoorthy, S., Alexandrov, T., Becker, M., Bretschneider, T., Buerkert, A., Crecelius, A. C., Waele, D. D., Elsen, A., Heckel, D. G., Heklau, H., Hertweck, C., Kai, M., Knop, K., Krafft, C., Maddula, R. K., Matthäus, C., Popp, J., Schneider, B., Schubert, U. S., Sikora, R. A., Svatoˇ s, A. s. and Swennen, R. L. (2014). Phenalenone-type phytoalexins mediate resistance of banana plants (Musa spp.) to the burrowing nematode Radopholus similis. Proceedings of the National Academy of Sciences *111*, 105–110.

Im, W., Feig, M. and Brooks, C. L. (2003). An implicit membrane generalized born theory for the study of structure, stability, and interactions of membrane proteins. Biophys J *85*, 2900–18.

Jensen, M. O., Jogini, V., Borhani, D. W., Leffler, A. E., Dror, R. O. and Shaw, D. E. (2012). Mechanism of voltage gating in potassium channels. Science *336*, 229–233.

Jiang, Y., Lee, A., Chen, J., Ruta, V., Cadene, M., Chait, B. T. and MacKinnon, R. (2003). X-ray structure of a voltage-dependent K+ channel. Nature *423*, 33–41.

Jo, S., Kim, T., Iyer, V. G. and Im, W. (2008). CHARMM-GUI: a web-based graphical user interface for CHARMM. J Comput Chem *29*, 1859–65.

Jung, H. J., Lee, J. Y., Kim, S. H., Eu, Y.-J. J., Shin, S. Y., Milescu, M., Swartz, K. J. and Kim, J. I. (2005). Solution structure and lipid membrane partitioning of VSTx1, an inhibitor of the KvAP potassium channel. Biochemistry *44*, 6015–23.

Khalili-Araghi, F., Jogini, V., Yarov-Yarovoy, V., Tajkhorshid, E., Roux, B. and Schulten, K. (2010). Calculation of the gating charge for the Kv1.2 voltage-activated potassium channel. Biophys J *98*, 2189–98.

Labro, A. J., Raes, A. L., Bellens, I., Ottschytsch, N. and Snyders, D. J. (2003). Gating of Shaker-type Channels Requires the Flexibility of S6 Caused by Prolines. Journal of Biological Chemistry *278*, 50724–50731.

Labro, A. J. and Snyders, D. J. (2012). Being flexible: the voltage-controllable activation gate of kv channels. Front Pharmacol *3*, 168.

Lacroix, J. J. and Bezanilla, F. (2011). Control of a final gating charge transition by a hydrophobic residue in the S2 segment of a K+ channel voltage sensor. Proceedings of the National Academy of Sciences *108*, 6444–6449.

Lainé, M., Lin, M.-c. A. C., Bannister, J. P. A., Silverman, W. R., Mock, A. F., Roux, B. and Papazian, D. M. (2003). Atomic proximity between S4 segment and pore domain in Shaker potassium channels. Neuron *39*, 467–81.

Lampe, R. A., Defeo, P. A., Davison, M. D., Young, J., Herman, J. L., Spreen, R. C., Horn, M. B., Mangano, T. J. and Keith, R. A. (1993). Isolation and pharmacological characterization of omega-grammotoxin SIA, a novel peptide inhibitor of neuronal voltage-sensitive calcium channel responses. Molecular pharmacology *44*, 451–460.

Larsson, H. P., Baker, O. S., Dhillon, D. S. and Isacoff, E. Y. (1996). Transmembrane movement of the shaker K+ channel S4. Neuron *16*, 387–97.

Lee, C. W., Kim, S., Roh, S. H., Endoh, H., Kodera, Y., Maeda, T., Kohno, T., Wang, J. M., Swartz, K. J. and Kim, J. I. (2004). Solution structure and functional characterization of SGTx1, a modifier of Kv2.1 channel gating. Biochemistry *43*, 890–7.

Li-Smerin, Y. and Swartz, K. J. (2000). Localization and molecular determinants of the Hanatoxin receptors on the voltage-sensing domains of a K+ channel. The Journal of general physiology *115*, 673–684.

Lin, M.-c. A. C., Abramson, J. and Papazian, D. M. (2010). Transfer of ion binding site from ether-a-go-go to Shaker: Mg2+ binds to resting state to modulate channel opening. J Gen Physiol *135*, 415–31.

Long, S. B., Campbell, E. B. and MacKinnon, R. (2005a). Voltage Sensor of Kv1.2: Structural Basis of Electromechanical Coupling. Science *309*, 903–908.

Long, S. B., Campbell, E. B. and MacKinnon, R. (2005b). Crystal structure of a mammalian voltage-dependent Shaker family K+ channel. Science *309*, 897–903.

Long, S. B., Tao, X., Campbell, E. B. and MacKinnon, R. (2007). Atomic structure of a voltage-dependent K+ channel in a lipid membrane-like environment. Nature *450*, 376–82.

MacKerell, . A. D., Bashford, D., Bellott, Dunbrack, . R. L., Evanseck, J. D., Field, M. J., Fischer, S., Gao, J., Guo, H., Ha, S., Joseph-McCarthy, D., Kuchnir, L., Kuczera, K., Lau, F. T. K., Mattos, C., Michnick, S., Ngo, T., Nguyen, D. T., Prodhom, B., Reiher, W. E., Roux, B., Schlenkrich, M., Smith, J. C., Stote, R., Straub, J., Watanabe, M., Wiórkiewicz-Kuczera, J., Yin, D. and Karplus, M. (1998). All-Atom Empirical Potential for Molecular Modeling and Dynamics Studies of Proteins†. J Phys Chem B *102*, 3586–3616.

Milescu, M., Vobecky, J., Roh, S. H., Kim, S. H., Jung, H. J., Kim, J. I. and Swartz, K. J. (2007). Tarantula toxins interact with voltage sensors within lipid membranes. J Gen Physiol *130*, 497–511.

Papazian, D. M., Timpe, L. C., Jan, Y. N. and Jan, L. Y. (1991). Alteration of voltage-dependence of Shaker potassium channel by mutations in the S4 sequence. Nature *349*, 305–10.

Patapati, K. K. and Glykos, N. M. (2011). Three force fields' views of the 3(10) helix. Biophys J *101*, 1766–71.

Payandeh, J., Scheuer, T., Zheng, N. and Catterall, W. A. (2011). The crystal structure of a voltage-gated sodium channel. Nature *475*, 353–8.

Phillips, J. C., Braun, R., Wang, W., Gumbart, J., Tajkhorshid, E., Villa, E., Chipot, C., Skeel, R. D., Kalé, L. and Schulten, K. (2005). Scalable molecular dynamics with NAMD. J Comput Chem *26*, 1781–802.

Posokhov, Y. O., Gottlieb, P. A., Morales, M. J., Sachs, F. and Ladokhin, A. S. (2007). Is lipid bilayer binding a common property of inhibitor cysteine knot ion-channel blockers? Biophys J *93*, L20–2.

Rodriguez, B. M., Sigg, D. and Bezanilla, F. (1998). Voltage Gating of Shaker K+ Channels. The Journal of General Physiology *112*, 223–242.

Ruta, V., Chen, J. and MacKinnon, R. (2005). Calibrated measurement of gating-charge arginine displacement in the KvAP voltage-dependent K+ channel. Cell *123*, 463–75.

Ruta, V. and MacKinnon, R. (2004). Localization of the voltage-sensor toxin receptor on KvAP. Biochemistry *43*, 10071–9.

Sasaki, M., Takagi, M. and Okamura, Y. (2006). A Voltage Sensor-Domain Protein Is a Voltage-Gated Proton Channel. Science *312*, 589–592.

Schmidt, D. and MacKinnon, R. (2008). Voltage-dependent K+ channel gating and voltage sensor toxin sensitivity depend on the mechanical state of the lipid membrane. Proceedings of the National Academy of Sciences *105*, 19276–19281.

Schoppa, N. E. and Sigworth, F. J. (1998). Activation of Shaker Potassium Channels. The Journal of General Physiology *111*, 313–342.

Schow, E. V., Freites, J. A., Nizkorodov, A., White, S. H. and Tobias, D. J. (2012). Coupling between the voltage-sensing and pore domains in a voltage-gated potassium channel. Biochim Biophys Acta *1818*, 1726–36.

Schwaiger, C. S., Liin, S. I., Elinder, F. and Lindahl, E. (2013). The conserved phenylalanine in the K+ channel voltage-sensor domain creates a barrier with unidirectional effects. Biophys J *104*, 75–84.

Seoh, S. A., Sigg, D., Papazian, D. M. and Bezanilla, F. (1996). Voltage-sensing residues in the S2 and S4 segments of the Shaker K+ channel. Neuron *16*, 1159–67.

Sigworth, F. J. (1994). Voltage gating of ion channels. Q Rev Biophys *27*, 1–40.

Swartz, K. J. (2004). Towards a structural view of gating in potassium channels. Nature Reviews Neuroscience *5*, 905–916.

Swartz, K. J. and MacKinnon, R. (1995). An inhibitor of the Kv2. 1 potassium channel isolated from the venom of a Chilean tarantula. Neuron *15*, 941–949.

Tao, X., Lee, A., Limapichat, W., Dougherty, D. A. and MacKinnon, R. (2010). A gating charge transfer center in voltage sensors. Science *328*, 67–73.

Tombola, F., Pathak, M. M. and Isacoff, E. Y. (2006). How does voltage open an ion channel? Annu Rev Cell Dev Biol *22*, 23–52.

Vargas, E., Bezanilla, F. and Roux, B. (2011). In search of a consensus model of the resting state of a voltage-sensing domain. Neuron *72*, 713–20.

Vargas, E., Yarov-Yarovoy, V., Khalili-Araghi, F., Catterall, W. A., Klein, M. L., Tarek, M., Lindahl, E., Schulten, K., Perozo, E., Bezanilla, F. and Roux, B. (2012). An emerging consensus on voltage-dependent gating from computational modeling and molecular dynamics simulations. J Gen Physiol *140*, 587–94.

Vieira-Pires, R. S. a. and Morais-Cabral, J. a. H. (2010). 310 helices in channels and other membrane proteins. The Journal of General Physiology *136*, 585–592.

Wang, J., Cieplak, P. and Kollman, P. A. (2000). How well does a restrained electrostatic potential (RESP) model perform in calculating conformational energies of organic and biological molecules? Journal of Computational Chemistry *21*, 1049–1074.

Wang, J. M., Roh, S. H., Kim, S., Lee, C. W., Kim, J. I. and Swartz, K. J. (2004). Molecular surface of tarantula toxins interacting with voltage sensors in Kv channels. The Journal of general physiology *123*, 455–467.

White, S. H. (2013). Membrane Proteins of Known 3D Structure. http://blanco.biomol.uci.edu/mpstruc/ (accessed January 2, 2014).

Wojtas-Niziurski, W., Meng, Y., Roux, B. T. and Berneche, S. (2013). Self-learning adaptive umbrella sampling method for the determination of free energy landscapes in multiple dimensions. Journal of chemical theory and computation *9*, 1885–1895.

Wood, W. F. (1990). New components in defensive secretion of the striped skunk,Mephitis mephitis. Journal of Chemical Ecology *16*, 2057–2065.

Xu, Y., Ramu, Y. and Lu, Z. (2008). Removal of phospho-head groups of membrane lipids immobilizes voltage sensors of K+ channels. Nature *451*, 826–829.

Yarov-Yarovoy, V., DeCaen, P. G., Westenbroek, R. E., Pan, C. Y., Scheuer, T., Baker, D. and Catterall, W. A. (2012). Structural basis for gating charge movement in the voltage sensor of a sodium channel. Proceedings of the National Academy of Sciences *109*, E93–E102.

Yeheskel, A., Haliloglu, T. and Ben-Tal, N. (2010). Independent and cooperative motions of the Kv1.2 channel: voltage sensing and gating. Biophys J *98*, 2179–88.

Yifrach, O. and MacKinnon, R. (2002). Energetics of pore opening in a voltage-gated K(+) channel. Cell *111*, 231–9.

Zagotta, W. N., Hoshi, T., Dittman, J. and Aldrich, R. W. (1994). Shaker potassium channel gating. II: Transitions in the activation pathway. J Gen Physiol *103*, 279–319.

Zhou, Y., Morais-Cabral, J. H., Kaufman, A. and MacKinnon, R. (2001). Chemistry of ion coordination and hydration revealed by a K+ channel-Fab complex at 2.0 A resolution. Nature *414*, 43–8.